A Molecular Recognition Feature mediates ribosome-induced SRP-receptor assembly in protein targeting

Yu-Hsien Hwang Fu, Sowmya Chandrasekar, Jae Ho Lee, and Shu-ou Shan*

Division of Chemistry and Chemical Engineering, California Institute of Technology, Pasadena, California, USA

* Corresponding author. Email: sshan@caltech.edu

Key words: Signal Recognition Particle; ribosome; protein targeting; Molecular Recognition Feature; intrinsically disordered protein

Short running title: A MoRF element activates SRP-receptor assembly

eTOC Summary

Hwang Fu et al show that a Molecular Recognition Feature (MoRF) in the mammalian signal recognition particle (SRP) receptor accelerates SRP-receptor assembly in response to the ribosome. The MoRF functionally replaces the bacterial SRP RNA to sense cargo loading and activate cotranslational protein targeting.

Abstract

Molecular Recognition Features (MoRFs) provide interaction motifs in intrinsically disordered protein regions to mediate diverse cellular functions. Here we report that a MoRF element, located in the disordered Linker domain of the mammalian signal recognition particle (SRP) receptor and conserved among eukaryotes, plays an essential role in sensing the ribosome during co-translational protein targeting to the endoplasmic reticulum. Loss of the MoRF in the SRP receptor (SR) largely abolishes the ability of the ribosome to activate SRP-SR assembly and impairs co-translational protein targeting. These results demonstrate a novel role for MoRF elements and provide a mechanism for the ribosome-induced activation of the mammalian SRP pathway. Kinetic analyses and comparison with the bacterial SRP further suggest that the SR MoRF functionally replaces the essential GNRA tetraloop in the bacterial SRP RNA, providing an example for the replacement of RNA function by proteins during the evolution of ancient ribonucleoprotein particles.

Introduction

Signal Recognition Particle (SRP) is a universally conserved targeting machine that co-translationally delivers the majority of membrane and secretory proteins, which compose nearly 30% of the proteome, to the eukaryotic endoplasmic reticulum (ER) or the bacterial plasma membrane (Zhang & Shan 2014; Akopian et al. 2013). Targeting initiates when SRP recognizes an N-terminal signal sequence or the first transmembrane domain of a nascent polypeptide emerging from the ribosome exit tunnel. The interaction of SRP with the SRP receptor (SR) recruits the ribosome-nascent chain complex (RNC) to the target membrane, where the RNC is unloaded onto the Sec61p (or SecYEG in bacteria) translocation machinery, and the nascent protein is integrated into or translocated across the membrane. The most conserved components of SRP and SR can be found in bacteria, where SRP is composed of a 4.5S RNA tightly bound to the SRP54 protein (named Ffh in bacteria). SRP54 contains a methionine-rich M-domain that binds signal sequences on the nascent polypeptide and a special GTPase, NG-domain that dimerizes with a homologous NG-domain in SR (named FtsY in bacteria). The GTP-dependent interaction of SRP with FtsY is extensively regulated by the signal sequence and 4.5S RNA in the bacterial SRP pathway to enable efficient and selective co-translational protein targeting (Zhang & Shan 2014; Shan 2016). Specifically, RNCs bearing a functional signal sequence pre-organizes SRP into a conformation in which the conserved GNRA tetraloop of the 4.5S RNA is positioned to contact a basic surface on the NG-domain of FtsY; this contributes a key interaction that enables the rapid recruitment of FtsY in response to recognition of the correct cargo (Zhang et al. 2008; Shen & Shan 2010; Shen et al. 2011).

SRP undergoes an extensive expansion in size and complexity during evolution. The eukaryotic SRP contains a larger 7SL RNA on which five additional protein subunits (SRP19,

SRP68/72 and SRP9/14) are assembled. Recent work showed that the interaction between mammalian SRP and SR is accelerated ~100-fold by the 80S ribosome and 20-fold by the signal sequence (Bacher et al. 1996; Mandon et al. 2003; Lee et al. 2018). The ribosome-induced stimulation is mammalian-specific, and its underlying molecular mechanism remains incompletely understood. Single-molecule measurements showed that the ribosome unlocks SRP from an auto-inhibited state and allows SRP to sample an active conformation that is conducive to SR binding (Lee et al. 2018). On the other hand, multiple studies implicated the eukaryotic SR in interaction with and sensing the ribosome (Fulga et al. 2001; Legate & Andrews 2003; Bacher et al. 1999; Mandon et al. 2003; Jadhav et al. 2015). While bacterial SR is a single protein in which the NG-domain is preceded by two amphiphilic lipid-binding helices, eukaryotic SR is a heterodimer of SRα and SRβ subunits. SRβ is a single-pass transmembrane protein anchored at the ER. SRα binds tightly to SRβ via its N-terminal X-domain, which is connected to the NG-domain through a ~200-residue intrinsically disordered Linker. Eukaryotic SR co-sediments with empty 80S ribosomes, and the SR Linker is important in mediating ribosome binding (Mandon et al. 2003). More recently, Jadhav et al. examined two charged segments in the SR Linker, CBR (residues 129-176) and RBR (residues 205-250) (Fig. 1A), and suggested that RBR is responsible for ribosome binding (Jadhav et al. 2015).

The importance of the SR linker reflects the expansion of intrinsically disordered protein regions (IDRs) in the proteome during the evolution from bacteria to higher eukaryotes (Ward et al. 2004; Oldfield et al. 2005). In contrast to the canonical structure-function paradigm, IDRs mediate critical cellular processes without assuming a preformed stable structure (Oldfield & Dunker 2014; Wright & Dyson 2015; Latysheva et al. 2015). IDRs are characterized by low sequence complexity, low conservation, and biased amino acid compositions that promote

disorder (Oldfield et al. 2005; Oldfield & Dunker 2014). These features often lead to low affinity, transient interactions of IDRs with their binding partners, allowing IDRs to mediate dynamic cellular processes such as signaling, complex assembly, or lipid-droplet formation (van der Lee et al. 2014). IDRs often exert their functions via Molecular Recognition Features (MoRFs), which provide interaction sites with binding partners (Mohan et al. 2006; Mészáros et al. 2009; Disfani et al. 2012; Fang et al. 2013; Cumberworth et al. 2013; Fung et al. 2018). MoRFs are short (10-70 residues) segments in IDRs that undergo disorder-to-order transitions upon binding and have been proposed to help recruit interaction partners to an IDR-mediated molecular hub (Oldfield et al. 2008). However, the disordered nature of IDRs presents major challenges to the elucidation of their structure, dynamics and activity, and more work is needed to understand the mechanistic principle by which MoRFs mediate diverse cellular functions.

In this study, we used the recently reconstituted human SRP and SR to examine the mechanism by which the mammalian SR senses and responds to the 80S ribosome during co-translational protein targeting. We identified a conserved MoRF element in the disordered SR Linker and showed that it is responsible for accelerating SRP-SR assembly in response to the ribosome. The role of this MoRF element phenocopies that of the GNRA tetraloop in the bacterial 4.5S RNA, which accelerates SRP-FtsY assembly in response to the RNC, whereas the corresponding tetraloop in the mammalian 7SL RNA has lost this stimulatory role. We propose that the MoRF element in mammalian SR functionally replaces the electrostatic tether provided by the bacterial 4.5S RNA during SRP-SR interaction. This and other observations suggest that many functions of the bacterial SRP RNA have been replaced by protein subunits during the evolution of this ancient ribonucleoprotein particle.

Results

A MoRF element in the SR Linker is important for SR function.

The SR Linker contains ~200 residues and is intrinsically disordered. Based on charge distribution and evolutionary conservation, a previous work suggested the presence of two functional segments in the SR Linker, CBR (residue 129-176) and RBR (residue 205-250), proposed to regulate the Sec61□-Sec62 interaction and to bind the ribosome, respectively (Jadhav et al. 2015). To identify potential interaction motifs, we analyzed the SR linker sequence using multiple MoRF predictors including ANCHOR, MoRFpred, and MFSPSSMPred (Mészáros et al. 2009; Disfani et al. 2012; Fang et al. 2013). The three algorithms are based on very different approaches. ANCHOR uses a scoring function that estimates the likelihood of sequences to undergo folding upon binding of globular partners. MoRFpred uses a machine-learning algorithm to make predictions based on sequence properties including evolutionary conservation, predicted disorder, and selected physicochemical properties of amino acids such as hydrophobicity and charge. MFSPSSMPred uses an algorithm similar to MoRFpred, but the sequences are pre-filtered for conservation. All three programs converged on a predicted MoRF at residues 242-261 (Fig. 1A). Sequence alignments of SR□ from diverse species also showed that the MoRF is the most conserved sequence in the SR Linker (Fig. 1B and S1).

To dissect the functions of the various segments in the SR Linker, we generated a set of linker deletion mutants SRdL, SRdC, SRdR, and SRdM in which the entire Linker, CBR, RBR and MoRF are replaced with $(GS)_6$, respectively (Fig. 1C). For *in vitro* assays, we used a functional soluble SR construct, SR□□□TM, in which the dispensable N-terminal transmembrane domain of SR□ is removed (Fig. 1C; (Ogg et al. 1998; Lee et al. 2018)). We first

tested these mutants in a co-translational protein targeting assay, which examines the ability of recombinant, purified SRP and SR to mediate the targeting and insertion of a model SRP substrate, preprolactin (pPL), into ER microsomes. The microsomes were trypsinized and salt-washed (TKRM) to deplete endogenous SRP and SR (see **Methods**). Deletion of the SR Linker severely disrupted the targeting and translocation of pPL (Fig. 1C, 1D). Unexpectedly, despite having the smallest deletion in the SR Linker, SRdM displayed a stronger defect in SRP-dependent pPL targeting than SRdC and SRdR (Fig. 1C, D), indicating that the MoRF element contains residues essential for SR function.

To further dissect the potential interactions of the MoRF, we mutated conserved residues in this element (R246, W248, L259, and Y261) to alanines (Fig. 1B). Both mutants SR(RW/AA) and SR(LY/AA) exhibited modest defects in pPL targeting, and the combination of all four point mutations, SR(RWLY/4A), reproduced the targeting defect of SRdM (Fig. 1B, E). This result strongly suggests that the conserved aromatic and charged residues in the SR MoRF mediate key molecular interactions during SRP-dependent protein targeting.

The SR MoRF is important for co-translational protein targeting in yeast.

To test the role of SR MoRF *in vivo*, we leveraged the fact that this MoRF element, especially its functionally important RW/L residues identified above, is conserved across eukaryotic organisms including diverse yeast strains (Fig. 1B and S2A). Using CRISPR-Cas9 based gene editing, we introduced a $(GS)_6$ linker to replace the MoRF sequence (residues 208 – 230) of genomic *SRP101*, the yeast SR homologue, in *S. cerevisiae* strain BY4741 (see **Method**). A C-terminal FLAG tag was introduced into both *SRP101* and *srp101*^{dM} to facilitate measurement of SR expression levels. To minimize adaptation of yeast cells bearing mutations in

components of the SRP pathway (Mutka & Walter 2001; Ogg et al. 1992; Jiang et al. 2008), the *srp101*^{dM} strain was maintained in synthetic minimal media containing ethanol and glycerol (SCEG). We found that *srp101*^{dM} cells exhibited a significant growth defect compared to *SRP101* cells at both 30 °C and 37 °C (Fig. 2A and S2B), indicating that the SR MoRF is important for supporting yeast cell growth.

To test the effect of the SR MoRF deletion on SRP-dependent protein targeting, we measured the *in vivo* targeting and translocation of a model substrate DHC-F, in which the signal sequence of prepro--factor is replaced by the hydrophobic core of the dipeptidyl aminopeptidase B (DAP2) signal sequence to convert it into an SRP-dependent substrate protein (Fig. S2D; (Ng et al. 1996; Cho & Shan 2018)). DHC-F was efficiently glycosylated upon insertion into the ER (Rao et al. 2016; Wang et al. 2010; Yabal et al. 2003), providing a quantitative readout for its targeting and translocation. To measure the targeting kinetics of newly synthesized proteins, we carried out pulse-chase assays coupled to immunoprecipitation of HA-tagged substrate proteins (see **Method**; (Cho & Shan 2018)). The results showed that, while DHC-F was rapidly and nearly completely translocated in *SRP101* cells, the translocation of DHC-F was substantially delayed and plateaued at <50% in *srp101*^{dM} cells (Fig. 2B). Western blot analysis of yeast ER microsomes showed that the observed targeting defect was not due to lower level of ER-localized SR in *srp101*^{dM} compared to *SRP101* cells (Fig. S2C).

The following observations suggested additional defects in *srp101*^{dM} cells. In control reactions, we tested the insertion of a post-translationally targeted model protein substrate, BirA-Bos1, into the ER (Cho & Shan 2018). BirA-Bos1 is a model tail-anchored membrane protein substrate in which the transmembrane domain of the SNARE protein Bos1 is fused to the C-

terminus of BirA (Fig. S2D). Due to their topology, tail-anchored proteins are targeted post-translationally via SRP-independent pathways. A significant defect of ER targeting and insertion was also observed with BirA-Bos1 in *srp101*^{dM} cells (Fig. S2E), indicating a general defect in protein insertion into the ER. This is not surprising, as many translocation machineries at the ER are substrates of the SRP pathway; thus, defects of the SRP pathway in *srp101*^{dM} cells would compromise the biogenesis and function of ER in general. In western blot analysis, we also found that a fraction of Srp101p^{dM} was proteolyzed to a ~65 kD fragment (Fig. S2C). Although partial proteolysis of SR during ER isolation was well characterized (Meyer & Dobberstein 1980; Hortsch et al. 1985; Laufi'er et al. 1985) and the amount of proteolysis (<50%) was insufficient to account for the observed targeting defect of DHC-F, the higher proteolytic susceptibility of Srp101p^{dM} suggest a loss of contacts that protect the SR Linker. Together, these results show that the SR MoRF is conserved across eukaryotic organisms, and loss of this element leads to large and promiscuous protein translocation defects of the ER *in vivo*.

SR MoRF and the ribosome synergistically stimulate SRP-SR complex formation.

To understand the molecular mechanism by which the SR MoRF impacts the targeting reaction, we asked whether the SR MoRF plays a role in SRP-SR complex formation, the first molecular step that the SR participates in during protein targeting. To this end, we first tested the effect of the SR Linker mutations on the reciprocally stimulated GTPase reaction between SRP and SR (Fig. 3A). The GTPase activity of SRP and SR is stimulated 10^2-10^3 fold when they form a complex with one another, providing a convenient readout of their interaction (Peluso et al. 2001; Lee et al. 2018). Pre-steady-state fluorescence measurements of the SRP-SR interaction and comparison with the Michaelis-Menten kinetic constants of their stimulated GTPase reaction

showed that, at sub-saturating SR concentrations, the GTPase rate constant k_{cat}/K_M is rate-limited by and equal to the rate constant of SRP-SR complex assembly in both the bacterial and mammalian systems (Peluso et al. 2001; Lee et al. 2018). The rate constant at saturating SR concentrations, k_{cat}, reports on the rate of GTP hydrolysis from a stably formed SRP•SR complex (Fig. 3A). As the ribosome and signal sequence are required to activate the SRP-SR interaction (Lee et al. 2018), stimulated GTPase reactions between SRP and SR were measured in the presence of saturating 80S ribosome and engineered SRP(4A10L), in which the M-domain of SRP54 is fused to a 4A10L signal sequence. This generates a ribosome- and signal sequence-bound SRP that fully mimics the effect of the RNC in stimulating SRP-SR assembly (Lee et al. 2018).

To decipher the roles of the individual domains of SR in complex assembly, we further tested two SR domain deletion mutants in addition to the Linker mutations described above (Fig. 1C). SRNG contains only the most conserved NG-domain known to mediate dimerization with the homologous NG-domain in SRP54. In SRdX, the X-domain of SR is deleted, which also abolishes the SR-SR interaction (Fig. 1C). As reported recently, mutant SRdX is fully functional in mediating rapid recruitment of SR to ribosome and signal sequence-loaded SRP ((Lee et al. 2018) and Fig. 3B). In contrast, deletion of the SR Linker severely disrupted the SRP-SR interaction, reducing the value of k_{cat}/K_m >20-fold (Fig. 3B, C). The effects of SR Linker deletion were similar regardless of whether the SRX domain was present (Fig. 3, cf. SRNG versus SRdL), indicating that the linker sequence functions independently of the X domain complex (Fig. 3B, C). In contrast, the value of k_{cat} was affected <2-fold by these mutations (Fig. 3B, D), indicating that the SR Linker plays a crucial and specific role in efficient complex formation between SRP and SR, but does not substantially affect the GTPase activity of

the SRP•SR complex. Importantly, the MoRF deletion led to a similar defect as deletion of RBR or the entire SR Linker, reducing the k_{cat}/K_m values ~60-fold and the k_{cat} value ~3-fold (Fig. 4A & B, filled circles/bars). In contrast, deletion of CBR led to a modest defect, with a ~4-fold reduction in k_{cat}/K_m and no effects on k_{cat} (Fig. 4A & 4B, filled circles/bars). The similar defects of SRdL, SRdR, and SRdM in this assay strongly suggest that the MoRF element is primarily responsible for the role of SR Linker in stimulating efficient SRP-SR assembly.

To test whether the SR MoRF is involved in ribosome-induced stimulation of SRP•SR complex assembly, we measured the stimulated GTPase reactions of signal sequence-bound SRP with wildtype and mutant SRs in the absence of 80S ribosome (Fig. 4A & 4B, open circles/bars). Notably, while the ribosome strongly stimulated complex formation between SRP and wildtype SR (~25-fold, Fig. 4C), as reported (Lee et al. 2018), the stimulatory effect of the ribosome was much smaller, ~3-fold, in reactions with mutants SRdL, SRdR, and SRdM (Fig. 4C). The loss of ribosome-induced stimulation of SRP-SR assembly is similar between these three mutants, indicating that the MoRF element is primarily responsible for communication between the SR Linker and the ribosome. In contrast, the ribosome still had a 12-fold stimulatory effect in the reaction with SRdC, only ~2-fold reduced from that of the reaction with wildtype SR (Fig. 4C, blue vs black). These results show that the MoRF in SR Linker is a key element that mediates the ribosome-induced activation of SRP-SR complex formation.

MoRF mediates a transient interaction to stabilize the transition state of SRP-SR assembly.

To test whether the ribosome and MoRF also affect the equilibrium and kinetic stability of the SRP•SR complex, we used an established Förster Resonance Energy Transfer (FRET) assay based on a donor dye (Cy3B) labeled at SRP54(K47C) and an acceptor dye (Atto647N)

labeled at the C-terminus of SR. To improve the solubility of labeled SR for fluorescence measurements, we used the SRdX construct in which the SR X-domain and SR are removed (Fig. S3A). As previously reported, SRdX displayed SRP-SR assembly, GTPase activation, and preprotein targeting activities that are comparable to or slightly higher than SR TM, and therefore provides a fully functional mimic of SR for studying the initial assembly between SRP and SR (Lee et al. 2018). We also confirmed that the Linker deletion mutants (SRdC, SRdR, and SRdM) in the SRdX background had the same effects on the stimulated GTPase reaction as in SRαβΔTM (Fig. S3B). This validated the usage of the SRdX constructs to study the role of the MoRF in the fluorescence experiments below.

We first measured the dissociation rate constant (k_{off}) of the SRP•SR complex. In the presence of the ribosome, deletion of the MoRF enhanced rather than reduced the kinetic stability of the SRP•SR complex, slowing complex dissociation ~20-fold (Fig. 5A & 5B, filled circles/bars). In the absence of the ribosome, however, the MoRF did not significantly affect the kinetic stability of the SRP•SR complex (Figs. 5A & 5B, open circles/bars). The effects of the SRdM mutation on SRP•SR complex dissociation rates as well as the synergistic effect of this mutation with the 80S ribosome closely resemble those observed during SRP-SR association (cf Fig. 5B vs 4B). Equilibrium titrations using this FRET assay (Fig. S3C) further revealed that the SRdM mutation modestly weakened the SRP•SR complex, displaying an equilibrium dissociation constant (K_d) 10-fold larger than that of wildtype SR in the presence of the ribosome (Fig. 5C, D). In the absence of the ribosome, the mutational effect on K_d is smaller (2-fold), reflecting a modest synergy between the MoRF and the ribosome in enhancing the equilibrium stability of the SRP•SR complex (Fig. 5C, D).

Attempts to measure the SRP-SR association rate constants (k_{on}) using the FRET assay were unsuccessful with SRdM, because the mutant SR co-aggregated with ribosome at concentrations above 1-2 μM. We therefore calculated k_{on} from the experimentally determined k_{off} and K_d values ($k_{on} = k_{off}/K_d$). The calculated k_{on} values are in reasonable agreement with the values of k_{cat}/K_m measured from the GTPase reaction and corroborated the conclusions from the enzymatic assay, that is, mutant SRdM slowed SRP-SR association specifically in the presence of the ribosome, and lost most of the ribosome-mediated activation of during this step (Fig. 5D).

Collectively, these results show that the SR MoRF strongly accelerates both complex assembly between SRP and SR (~200-fold), while exerting more modest effects on the kinetic and equilibrium stability of the SRP•SR complex (10-20 fold). Moreover, all the stimulatory effects of the SR MoRF are largely abolished in the absence of the ribosome. Thus, the MoRF element and 80S ribosome act synergistically to stabilize the transition state during SRP•SR complex formation.

The MoRF does not directly mediate ribosome binding to SR.

The simplest molecular model to explain the synergistic effects of the MoRF and 80S is that MoRF directly recruits the 80S ribosome. To test this model, we examined the effects of SR linker mutations on 80S binding using a co-sedimentation assay (Fig. 6 & S4). Deletion of either the CBR or RBR led to >2-fold reductions in SR-80S binding (Fig. 6A, C). The folded domains in SR, X□ and NG, also displayed no detectable 80S binding (Fig. 6B, C). In contrast, mutant SRdX lacking the X□ domain complex retained significant ribosome binding. These results suggest that the SR Linker is primarily responsible for the interaction of SR with the 80S ribosome, and that both the CBR and RBR in this linker provide important ribosome binding

sites. In contrast to the CBR and RBR deletions, deletion of the MoRF led to minimal loss in the 80S binding of SR (Fig. 6A, C). Thus, the MoRF does not directly recruit the ribosome to SR.

The electrostatic tethering of SRP RNA to SR is lost in the mammalian SRP pathway

Previous work with the bacterial SRP showed that the conserved GNRA tetraloop of the 4.5S RNA forms an electrostatic interaction with a basic surface on the FtsY NG-domain, providing a transient tether that holds SRP and FtsY together to stabilize the transition state of their assembly (Fig. 7A left; (Zhang et al. 2008; Shen & Shan 2010; Shen et al. 2011)). The kinetic signatures of the SR MoRF are highly reminiscent of those of the 4.5S RNA tetraloop: both elements accelerate the association and dissociation of the SRP•SR complex, with a much smaller impact on the equilibrium stability of the complex (Shen et al. 2011). Moreover, both the SR MoRF and 4.5S RNA tetraloop specifically exert their stimulatory effects in response to the RNC (Shen et al. 2011). The GNRA tetraloop is conserved in the mammalian 7SL RNA. We therefore asked if the electrostatic tethering interaction between this RNA tetraloop and SR is preserved in the mammalian SRP pathway (Fig. 7A right).

To address this question, we assembled SRPs carrying mutations in the GNRA tetraloop and tested their effects on SRP-SR assembly using the stimulated GTPase assay between SRP and SR. In bacterial SRP, mutation of the RNA tetraloop from GGAA to UUCG reduces the value of k_{cat}/K_m ~200-fold (Zhang et al. 2008). Even modest mutations, such as GUAA and GUCG, led to ~20-fold and ~50-fold reductions in k_{cat}/K_m, respectively (Fig. 7B, *E. coli*). In contrast, the k_{cat}/K_m value for the reaction of human SRP with SR was minimally affected by any of these tetraloop mutations (Fig. 7B, Mammalian and S5A). Consistent with the results of the GTPase assays, none of the 7SL tetraloop mutations significantly impair the targeting of pPL to

ER microsomes (Fig. S5B), in contrast to the deleterious effects of the same mutations in the 4.5S RNA (Zhang et al. 2008).

Comparison of the crystal structures of the bacterial and human SRP•SR NG-domain complex further showed that the cluster of basic residues (K399, R402, and K406) on FtsY that comprise the positively charged surface for interaction with the 4.5S RNA tetraloop is reduced to a single K537 in mammalian SR (Fig. S5C). Moreover, while mutation of K399 in FtsY reduced the rate of SRP-FtsY complex formation ~100-fold (Fig. 7C, *E. coli*; (Shen & Shan 2010)), mutation of the corresponding K537 in mammalian SR had a <5-fold effect on the rate of SRP-SR assembly (Fig. 7C, Mammalian and S5D). Together, these results show that the mammalian SRP pathway no longer uses the electrostatic tether between the RNA tetraloop and the basic cluster in SRNG to enable rapid SRP•SR complex formation. Instead, the role of the 4.5S RNA tetraloop is phenocopied by the MoRF element in the SR linker.

Discussion

In this work, we identified and characterized a highly conserved MoRF element in the disordered Linker domain of mammalian SR that specifically accelerates SRP•SR complex assembly in response to the ribosome during co-translational protein targeting. Deletion or mutations of the SR MoRF led to severe defects in protein targeting and translocation to the ER *in vitro* and *in vivo*, and resulted in strong growth defects in yeast. Mechanistic dissections showed that the SR MoRF specifically stimulates the recruitment of SR to cargo-loaded SRP, and that its action is synergistic with that of the 80S ribosome. Intriguingly, the roles of the MoRF element in accelerating SRP-SR assembly phenocopy those of the GNRA tetraloop in the bacterial 4.5S RNA, whereas the corresponding RNA tetraloop in the mammalian SRP has lost this essential role.

The kinetic and equilibrium analyses in this work allowed us to construct a free energy diagram that describes the contributions of the ribosome and MoRF to SRP-SR complex formation in a formal model (Fig. 8A). In the presence of the ribosome, the MoRF specifically stabilizes the transition state of SRP-SR assembly ~3.2 kcal/mol. Both the association and dissociation of the SRP•SR complex are significantly accelerated by the MoRF, whereas the equilibrium of complex formation was affected by only ~1.4 kcal/mol (Fig. 8A, left, comparing black and red lines). The effects of the MoRF are largely lost in the absence of the ribosome (Fig. 8A, right, comparing black and red lines). Reciprocally, the ribosome stabilizes the transition state during complex formation with SRP ~3.1 kcal/mol, and has a smaller effect, ~0.7 kcal/mol, on the equilibrium of complex formation (WT, black line, comparing +80S and -80S); these stimulatory effects of the ribosome are largely abolished upon deletion of the MoRF (dM, red line, comparing +80S and -80S). Thus, the SR MoRF and the 80S ribosome synergistically

activate the assembly between SRP and SR, and they exert their effects specifically during the transition state of complex formation.

Stimulation of SRP•SR complex assembly by the 80S ribosome is a eukaryote-specific phenomenon (Lee et al. 2018; Mandon et al. 2003; Bacher et al. 1996), as is the ability of the eukaryotic SR to directly bind the ribosome (Mandon et al. 2003; Jadhav et al. 2015). Based on the direct interaction of eukaryotic SR with the ribosome, it was proposed that the 80S ribosome, by contacting both the SRP and SR, could provide a template on which SRP and SR assemble (Mandon et al. 2003; Jadhav et al. 2015). However, the results here indicate that ribosome binding of free SR is largely uncorrelated with the efficiency of SRP•SR complex assembly or co-translational protein targeting. While SRdC and SRdR showed similarly low affinities for the ribosome, the stimulated GTPase and targeting activities of SRdC are much higher than those of SRdR. On the other hand, deletion of the SR MoRF had minimal impact on SR-ribosome binding, but severely disrupts SRP•SR complex assembly and co-translational protein targeting (c.f. Fig. 6C and Fig. 1D & 4B). These results ruled out the model that the SR MoRF exerts its stimulatory role by helping to recruit the ribosome. Instead, our results suggest that this element acts at a stage downstream of initial ribosome binding, specifically sensing and transmitting the information from the ribosome to the SRP and SR GTPases to activate their interactions. This could occur by optimizing the positioning of the SR NG-domain with respect to the SRP54-NG near the ribosome exit site to promote their assembly. The enrichment of conserved hydrophobic and aromatic residues in this MoRF also suggests that it participates in key, albeit transient, molecular interactions to exert this positioning effect. The precise interactions mediated by the MoRF remains to be determined.

Intriguingly, mutation of the MoRF in the mammalian SR Linker phenocopies the effects of mutations in the 4.5S RNA tetraloop in the bacterial SRP. Both elements (the eukaryotic SR MoRF and the bacterial SRP RNA tetraloop) specifically impact the transition state during SRP-SR assembly, with a much smaller effect on the equilibrium of complex formation (Peluso et al. 2000; Peluso et al. 2001; Zhang et al. 2008). The action of both elements are also strongly synergistic with the cargo (Shen & Shan 2010; Shen et al. 2011). In bacteria, the RNA tetraloop interacts with the basic surface on the FtsY NG-domain to form a transient electrostatic tether that stabilizes the transition state during complex assembly (Fig. 8B upper panel; (Shen & Shan 2010; Shen et al. 2011)). Mutation of either the charged residues in FtsY or the RNA tetraloop significantly impacts SRP and FtsY interactions (Fig. 7B & 7C, *E coli*; (Zhang et al. 2008; Shen & Shan 2010)). In contrast to the bacterial SRP, the assembly of mammalian SRP and SR is not sensitive to either of these mutations (Fig. 7B & 7C, Mammalian), indicating that the electrostatic tethering via the RNA tetraloop is no longer employed in the mammalian SRP system. Together with the similarities of the effects of SR MoRF and 4.5S RNA tetraloop, we propose that the mammalian SRP uses the SR MoRF in place of the RNA tetraloop to activate rapid SRP-SR assembly in response to cargo binding (Fig. 8B lower panel).

In addition to the SRP RNA tetraloop, the functions of multiple other elements in the bacterial SRP RNA are carried out by protein subunits in the eukaryotic SRP. For example, the eukaryote-specific SRP9/14 mediates interaction of the Alu-domain at the elongation factor binding site to regulate translation elongation, whereas the Alu-domain of SRP is comprised solely of RNA in gram positive bacteria (Halic et al. 2006; Beckert et al. 2015; Mary et al. 2010). Additionally, in a recent structure of a 'pre-handover' mammalian RNC•SRP•SR ternary complex, the SRP•SR NG-domain complex moves to the distal site of 7SL RNA after their

initial assembly and forms a network of interactions with SRP68/72 and the X□-domain of SR (Kobayashi et al. 2018). The analogous distal site docking of the NG-domain complex in bacterial SRP is mediated exclusively by interactions with the 4.5S RNA (Ataide et al. 2011). Collectively, these observations support a model in which multiple functions of the SRP RNA in this ancient ribonucleoprotein particle have been replaced by protein subunits during its evolution in higher eukaryotic organisms. MoRF elements in IDRs could play an important role in this process, by virtue of their ability to mediate weak, transient, but specific interactions encoded by their sequence, structural, and dynamic properties.

Material and Methods

Vector, protein and RNA preparations. Plasmids for recombinant expression of SRP protein and RNA subunits, SR□□□TM, and SRdX have been described (Lee et al. 2018). In brief, hSRP19 and hSRP54-4A10L were expressed in Rossetta pLyS cells using pET15b-h19 and pET23d-h54-4A10L, respectively. hSRP9 and hSRP14 were expressed separately in BL21(DE3)pLysS using pET3b-h9 and pET9a-h14, respectively, and purified as hSRP9/14 complex by combining the clarified lysates. hSRP68 and hSRP72 were co-expressed in BCY123 yeast cells using pRS426-h68/72 vector. pS7CA was used for *in vitro* transcription of the 7SL SRP RNA. For SR□□□TM, SR□ and SR□□TM were co-expressed in BL21(DE3*) cells using pET28a-hSR□ and pET15b-SR□□TM, respectively. SRdX was expressed using pET28a-hSR□(130-639). Plasmids for expression of mutant SRs and mutant 7SL RNAs were constructed using the QuikChange mutagenesis protocol (Stratagene). SRdC, SRdR, SRdM, and SRdL have residues 129-176, 205-250, 242-261, and 131-301 replaced with $(GS)_6$, respectively. Recombinant wildtype and mutant

SRs were expressed from *E. coli* and purified as previously described (Lee et al. 2018). Reconstituted SRP and SRP(4A10L) were assembled from individually expressed/purified SRP proteins and *in vitro* transcribed/gel purified 7SL RNA as described in the previous study (Lee et al. 2018). 80S ribosomes were purified from Rabbit Reticulocyte Lysate (RRL) as described in (Lee et al. 2018). Preprolactin (pPL) mRNA for *in vitro* translation-translocation assays were synthesized by *in vitro* transcription using SP6 polymerase following the Megascript protocol (Ambion). Cyslite SRP54(K47C) was labeled with Cy3B maleimide (Invitrogen) and purified as described (Lee et al. 2018). SRdX and SRdX(R458A) were labeled at the C-terminus with Atto647N (Invitrogen) via sortase mediated ligation, as described in (Lee et al. 2018). SR were centrifuged at 4 °C, 100,000 rpm in TLA100 rotor (Beckman Coulter) for 30 minutes to remove aggregates prior to all biochemical experiments,.

Co-translational targeting and translocation assay. Assays were carried out as described (Lee et al. 2018). Briefly, 8.5 µL of *in vitro* translation reactions of preprolactin in Wheat Germ extract (Promega) containing ^{35}S-methionine were initiated and, within 3 minutes, added to a mixture of 30 nM SRP, 0, 5, 10, 40, 100 nM wildtype or mutant SR, and 0.5 eq/µL of salt-washed, trypsin-digested microsomal membrane (TKRM) to a total volume of <13.5 µL. Reactions were quenched by addition of 2X SDS-loading buffer and boiling after 40 minutes, and analyzed by SDS-PAGE and autoradiography. The efficiency of translocation was quantified from Equation 1, in which 'PL' and 'pPL' are the integrated intensities for prolactin and preprolactin bands from autoradiography.

$$\%\text{Translocation} = \frac{\text{PL}}{\text{PL} + \frac{7}{8}\times\text{pPL}} \times 100 \qquad \text{(Eq. 1)}$$

Construction of SRP101FLAG and srp101^{dM}FLAG strains. Genomic *SRP101* in strain BY4741 was replaced with *SRP101-FLAG* or *srp101^{dM}-FLAG* (denoted as *SRP101* and *srp101^{dM}* in the main text) using CRISPR-Cas9 genome editing (Ryan et al. 2016). First, a DNA fragment containing the *SRP101* ORF and the flanking 5'UTR (524bp) and 3'UTR (184bp) was amplified from yeast genomic DNA (BY4741) and cloned into the pUC19 vector. To insert a C-terminal FLAG tag, pCAS-sgRNA^{FLAG} plasmid encoding *S. pyogenes* Cas9 and single guide RNA (sgRNA) containing a 20 bp reverse guide sequence (5'-TTGTTGAATAACATTGTCTG-3') that targets the sequence 36 bp downstream of the *SRP101* ORF.was cloned. The guide sequence was designed using Benchling CRISPR analysis tool. A flexible linker sequence (GSGAASG) followed by 1xFLAG sequence (DYKDDK) was inserted at the C-terminus of the *SRP101* coding sequence in pUC19, and asynonymous codon substitutions were inserted in the region targeted by the guide sequence using QuickChange Mutagenesis (Stratagen). The resulting plasmid was used to amplify a DNA repair fragment containing the SRP101-FLAG coding sequence and ~100 bp of the 3'UTR downstream of the sgRNA^{FLAG} site. pCAS-sgRNA^{FLAG} plasmid and the linear repair fragment were co-transformed into freshly prepared BY4741 competent cells and grown on YPD+G418 plates at 30 °C. Multiple single colonies were cultured and streaked on YPD to ensure the loss of pCAS-sgRNA^{FLAG} plasmid. The *SRP101-FLAG* strain was verified using PCR and DNA sequencing.

To generate the *srp101^{dM}-FLAG* strain, pCAS-sgRNA^{dM} plasmid encoding a guide RNA sequence (5'-GTTGGTAGTGGGAGAAAGTG-3') was designed to target nucleotide 626 in the *SRP101* coding sequence (5 bp into the MoRF region). To prepare the repair DNA fragment, the coding sequence for the MoRF (residues 208-230) in pUC19-SRP101-FlAG was by replaced by that for a $(GS)_6$ linker, and synonymous codon substitutions were introduced at the sequence

targeted by the sgRNA^{dM} guide sequence using QuickChange Mutagenesis (Stratagen). The *srp101^{dM}-FLAG* coding sequence and the flanking 5'UTR and 3'UTR was amplified to produce the linear repair DNA fragment. pCAS-sgRNA^{dM} plasmid and the linear repair fragment were co-transformed into the *SRP101-FLAG* strain and grown on YPD+G418 plates. To prevent adaptation of yeast cells to the MoRF deletion (Ogg et al. 1992; Mutka & Walter 2001), transformed colonies were picked as soon as they reached ~0.5 mm in diameter. All the subsequent culturing of *srp101^{dM} cells* were carried out in synthetic minimal media containing 2% ethanol and 2% glycerol (SCEG). The same procedure was used to generate a wild-type control *SRP101-FLAG* strain that contains the same synonymous mutation at the sgRNA^{dM} region as in the *srp101^{dM}-FLAG* strain. Both *SRP101-FLAG* and *srp101^{dM}-FLAG* strains were verified by DNA sequencing and were stored and grown in SCEG media unless otherwise specified.

Yeast growth assay. 2 mL cultures of *SRP101-FLAG* and *srp101^{dM}-FLAG* cells were grown at 30 °C in SCEG media to OD_{600} ~0.6. The cells were then diluted to OD_{600} ~0.1, and 2 μL aliquots of 10-fold serial dilutions were spotted onto YPD plates and incubated at 30 °C or 37 °C for 2 days.

In vivo pulse-chase assay. *SRP101-FLAG* and *srp101^{dM}-FLAG* cells were transformed with a pRS316 vector expressing either 3xHA-DHC□F or 3xHA-BirA-Bos1-Opsin under the GPD promoter. Transformed cells were grown in SCEG(-Ura) media to OD_{600} ~0.4. The cells were then washed and shifted to SD(-Ura) media and grown at 30 °C for 3.5 hours (Jiang et al. 2008). Yeast cells were harvested, washed in SD(-Ura-Cys-Met) media, resuspended in 1 mL SD(-Ura-Cys-Met) media to a final density of OD_{600} ~12, and incubated at 30 °C for 30 minutes. Cells

were pulse-labeled with 100 μCi/mL EasyTag™ EXPRESS35S protein labeling mix (Perkin Elmer) for 2 minutes and chased with 1mL SD(-Ura) media supplemented with 10 mM cold methionine and 0.5 mM cysteine. 400 μL aliquots were flash frozen in liquid nitrogen at indicated chase time points.

HA-tagged substrate proteins were immunoprecipitated as described previously (Cho & Shan 2018). In brief, individual aliquots of cells were harvested and treated with 0.3M NaOH for 3 minutes at room temperature, washed with water and lysed in lysis buffer (20 mM Tris-HCl pH 8.0, 150 mM NaCl, 2%SDS) by incubating at 65ºC for 15 minutes. Clarified lysate was diluted 20-fold in Anti-HA IP buffer (20 mM Tris-HCl pH 8.0, 150 mM NaCl, 1% TritonX-100) before loading on to pre-equilibrated Anti-HA magnetic beads (Thermo Fisher). Following incubation at room temperature for 10 minutes, the beads were washed with W1 (20 mM Tris-HCl pH 8.0, 150 mM NaCl, 1% TritonX-100, 2M Urea), W2 (20 mM Tris-HCl pH 8.0, 500 mM NaCl, 1% TritonX-100), W3 (20 mM Tris-HCl pH 8.0, 150 mM NaCl, 0.1% SDS), W4 (20 mM Tris-HCl pH 8.0, 150 mM NaCl). Proteins were eluted by adding 10 μl 1X SDS buffer and boiled for 5 minutes and analyzed by SDS PAGE and autoradiography. Translocation efficiency was quantified using Eq. 2, in which 'I_{Protein}' and 'I_{gProtein}' are the integrated intensities for the protein substrate and glycosylated protein bands, respectively.

$$\%\text{translocation} = \frac{I_{\text{gProtein}}}{I_{\text{gProtein}} + I_{\text{Protein}}} \times 100 \qquad \text{(Eq. 2)}$$

Western blot. Yeast microsomes were isolated from *SRP101-Flag* and *srp101^{dM}-Flag* strains as described (Rao et al. 2016). In brief, yeast spheroplasts were made by incubating harvested cells with 0.4 mg lyticase per units of OD_{600} of cells at 30°C for about 35 minutes in spheroplasts

buffer (50 mM HEPES pH 7.4, 2% glucose, 0.22 g/mL sorbitol, 0.01 g/mL yeast extract, 0.1 g/mL peptone). The spheroplast reaction was quenched on ice and cleaned up through a 1.5% Ficoll 400 cushion. The spheroplasts were resuspended in sorbitol lysis buffer (0.02g/mL sorbitol, 50 mM HEPES pH 7.4, 50 mM KOAc, 2 mM EDTA, 1mM DTT, 1x protease inhibitor cocktail) using a homogenizer. ER microsomes were then the purified from lysed spheroplasts through a 1M sucrose cushion. Purified and washed ER microsomes were pelleted, resuspended to a final concentration of 50-100U/mL, aliquoted and flash froze until ready. Microsome aliquots were boiled for 5 minutes in 2X SDS buffer immediately after thawing. 0.5 – 1 units of microsomes were analyzed by SDS-PAGE and immunoblotting using Anti-FLAG antibody (Genscript). IRDye® 800CW Goat anti-Mouse secondary antibody (LI-COR Biosciences) was used for visualization using an Odyssey imaging system.

GTPase assay. GTPase reactions were performed in SRP Assay Buffer (50 mM KHEPES (pH 7.5), 200 mM KOAc, 5 mM $Mg(OAc)_2$, 10% glycerol, 2 mM DTT, and 0.02% Nikkol) at 25 °C. Reactions were followed and analyzed as described before (Lee et al. 2018). The reciprocally stimulated GTPase reaction between SRP and SR were measured under multiple turnover conditions using 0.15 μM SRP(4A10L) and 0.2 μM 80S when indicated, varying concentrations of SR, and 100 μM GTP doped with trace γ-^{32}P-GTP (PerkinElmer). The SR concentration dependences of observed rate constants (k_{obsd}) were fit to Equation 3, where k_{cat} is the GTPase rate constant at saturating SR concentration, and K_m is the SR concentration required to reach half of the maximal observed GTPase rate constant.

$$k_{obsd} = k_{cat} \times \frac{[SR]}{K_m + [SR]} \qquad \text{(Eq. 3)}$$

Fluorescence FRET measurements. All reactions were measured in SRP Buffer supplemented with 0.03% BSA and 0.04% Nikkol at 25 °C. All fluorescence measurements used SRs carrying the R458A mutation, which specifically blocks GTP hydrolysis to enable measurements of the assembly and disassembly of SRP and SR in their GTP-bound state. The values of k_{off} were determined using pulse chase experiments on a stopped-flow apparatus (Kintek) with wildtype SR and a Fluorolog 3-22 spectrofluorometer (Jobin Yvon) with mutant SRs. The SRP•SR complex were preformed using 12.5 nM labeled SRP(4A10L) and 1 μM wildtype or mutant SR in the presence of 1 mM GTP, and 50 nM 80S when indicated. 8 μM unlabeled wildtype SR was added to initiate complex dissociation. Nonspecific fluorescence change was corrected by subtracting the background signal change measured in a parallel reaction in which the same volume of buffer was added. The time courses of fluorescence change were fit to Equation 4 (for wildtype SR in the presence of ribosome) or Equation 5 (for all other conditions) to extract the dissociation rate constants (k_{off}). F_{obsd} is the measured donor fluorescence signal, F_{AMP} is the corrected fluorescence change, F_0 is the initial fluorescence value at time zero, and t is time.

$$F_{obsd} = F_{AMP}(1 - \exp(-k_{off1} * t) - \exp(-k_{off2} * t)) + F_0 \qquad \text{(Eq. 4)}$$

$$F_{obsd} = F_{AMP}(1 - \exp(-k_{off} * t)) + F_0 \qquad \text{(Eq. 5)}$$

The equilibrium dissociation constants (K_d) of SRP•SR complexes were measured on a Fluorolog 3-22 spectrofluorometer. The equilibrium titrations were carried out using 12.5 nM Cy3B-labeled SRP, 1 mM GTP, and addition of increasing concentrations of Atto647N-labeled wildtype or mutant SR. Donor fluorescence was recorded when equilibrium is reached. The signal change was corrected by subtracting the background signal of a control titration with

unlabeled SR wildtype/mutants carried out in parallel. The fluorescence signal was converted to FRET efficiency (E) according to Equation 6,

$$E = 1 - \frac{F_{DA}}{F_{D0}} \quad \text{(Eq. 6)}$$

in which F_{D0} and F_{DA} are fluorescence signals in the absence and presence of the acceptor, respectively. The SR concentration dependences of E were fit to Equation 7 to extract the values of K_d. E_{max} is the value of E at saturating SR concentration.

$$E = E_{max} \times \frac{[SR]}{K_d + [SR]} \quad \text{(Eq. 7)}$$

SR-80S cosedimentation assay. Binding reactions were carried out in 50 mM KHEPES (pH 7.5), 100 mM KOAc, 5 mM $Mg(OAc)_2$ and 1 mM DTT at 25 °C. 400 nM SR were incubated with 150 nM 80S in a 50 µL reaction for 10 min. The mixture was loaded onto a 110 µL 1M sucrose cushion, and ultracentrifuged at 100K rpm for 2 hours in a TLA100 rotor (Beckman Coulter). The pellet fractions were resuspended in 20 µL 1X SDS loading buffer. Equal amounts of the Total and Pellet samples were analyzed on 10% SDS PAGE gels. The gels were coomassie-stained, scanned on a LI-COR Odyssey imager using a wavelength of 700 nm, and the intensities of the bands of interest were quantified. For SR-Xβ and SR-NG, which do not resolve well from ribosomal proteins, the N-terminally His_6-tagged SR bands were detected by western blot using anti-His_5 Mouse antibody (abcam) and IRDye® 800CW Goat anti-Mouse IgG (H + L) (LI-COR), and quantified on the LI-COR Odyssey imager.

Supplementary Information contains supplementary Figures 1-5 and figure legends.

Acknowledgements

We thank the Shan lab members for valuable suggestions, and H. Bernstein for sharing canine pancreatic microsomes. This work was supported by National Institutes of Health Grant GM078024 and Gordon and Betty Moore Foundation Grant GBMF2939 to S.-o.S..

Author contributions

Y.-H.H.F. and S.-o.S. designed research; Y.-H.H.F., S.C., and S.-o.S. performed research; Y.-H.H.F., S.C., and J.H.L., contributed new reagents/analytic tools; Y.-H.H.F., S.C., and S.-o.S. analyzed data; Y.-H.H.F. and S.-o.S. wrote the paper; S.-o.S. supervised the project.

Conflict of interest statement: The authors declare no competing financial interests.

References

Akopian, D. et al., 2013. Signal Recognition Particle: An Essential Protein-Targeting Machine. *Annu. Rev. Biochem.*, 82, pp.693–721.

Ataide, S.F. et al., 2011. The crystal structure of the signal recognition particle in complex with its receptor. *Science*, 331, pp.881–6.

Bacher, G. et al., 1996. Regulation by the ribosome of the GTPase of the signal-recognition particle during protein targeting. *Nature*, 381, p.248.

Bacher, G., Pool, M. & Dobberstein, B., 1999. The Ribosome Regulates the Gtpase of the β-Subunit of the Signal Recognition Particle Receptor. *J. Cell Biol.*, 146(4), p.723.

Beckert, B. et al., 2015. Translational arrest by a prokaryotic signal recognition particle is mediated by RNA interactions. *Nat. Struct. Mol. Biol.*, 22, pp.767–773.

Beitz, E., 2000. TEXshade: shading and labeling of multiple sequence alignments using LATEX2 epsilon. *Bioinformatics*, 16(2), pp.135–139.

Cho, H. & Shan, S., 2018. Substrate relay in an Hsp70-cochaperone cascade safeguards tail-anchored membrane protein targeting. *EMBO J.*, 37(16), p.e99264.

Cumberworth, A. et al., 2013. Promiscuity as a functional trait: intrinsically disordered regions as central players of interactomes. *Biochem. J.*, 454(3), pp.361–369.

Disfani, F.M. et al., 2012. MoRFpred, a computational tool for sequence-based prediction and characterization of short disorder-to-order transitioning binding regions in proteins. *Bioinformatics*, 28(12), pp.75–83.

Fang, C. et al., 2013. MFSPSSMpred: identifying short disorder-to-order binding regions in disordered proteins based on contextual local evolutionary conservation. *BMC Bioinformatics*, 14, p.300.

Fersht, A., 1999. *Structure and mechanism in protein science: A guide to enzyme catalysis and protein folding.*,

Fulga, T.A. et al., 2001. SRbeta coordinates signal sequence release from SRP with ribosome binding to the translocon. *EMBO J.*, 20(9), pp.2338–2347.

Fung, H.Y.J., Birol, M. & Rhoades, E., 2018. IDPs in macromolecular complexes: the roles of multivalent interactions in diverse assemblies. *Curr. Opin. Struct. Biol.*, 49, pp.36–43.

Halic, M. et al., 2006. Signal recognition particle receptor exposes the ribosomal translocon binding site. *Science*, 312(5774), pp.745–747.

Hortsch, M., Avossa, D. & Meyer, D.I., 1985. A structural and functional analysis of the docking protein. Characterization of active domains by proteolysis and specific antibodies. *J. Biol. Chem.*, 260(16), pp.9137–9145.

Jadhav, B. et al., 2015. Mammalian SRP receptor switches the Sec61 translocase from Sec62 to SRP-dependent translocation. *Nat. Commun.*, 6.

Jiang, Y. et al., 2008. An interaction between the SRP receptor and the translocon is critical during cotranslational protein translocation. *J. Cell Biol.*, 180(6), pp.1149 – 1161.

Kobayashi, K. et al., 2018. Structure of a prehandover mammalian ribosomal SRP·SRP receptor targeting complex. *Science*, 360(6386), pp.323–327.

Latysheva, N.S. et al., 2015. How do disordered regions achieve comparable functions to structured domains? *Protein Sci.*, 24(6), pp.909–922.

Laufi'er, L. et al., 1985. Topology of signal recognition particle receptor in the endoplasmic reticulum membrane. *Nature*.

Lee, J.H. et al., 2018. Sequential activation of human signal recognition particle by the ribosome and signal sequence drives efficient protein targeting. *Proc. Natl. Acad. Sci.*, 115(24), pp.5487–5496.
van der Lee, R. et al., 2014. Classification of intrinsically disordered regions and proteins. *Chem. Rev.*, 114(13), pp.6589–6631.
Legate, K.R. & Andrews, D.W., 2003. The β-Subunit of the Signal Recognition Particle Receptor Is a Novel GTP-binding Protein without Intrinsic GTPase Activity. *J. Biol. Chem.*, 278, pp.27712–27720.
Mandon, E.C., Jiang, Y. & Gilmore, R., 2003. Dual recognition of the ribosome and the signal recognition particle by the SRP receptor during protein targeting to the endoplasmic reticulum. *J. Cell Biol.*, 162(4), pp.575–585.
Mary, C. et al., 2010. Residues in SRP9/14 essential for elongation arrest activity of the signal recognition particle define a positively charged functional domain on one side of the protein. *RNA*, 16, pp.969–979.
Mészáros, B., Simon, I. & Dosztányi, Z., 2009. Prediction of Protein Binding Regions in Disordered Proteins. *PLoS Comput. Biol.*, 5(5).
Meyer, D.I. & Dobberstein, B., 1980. A membrane component essential for vectorial translocation of nascent proteins across the endoplasmic reticulum: requirements for its extraction and reassociation with the membrane. *J. Cell Biol.*, 87, pp.498–502.
Mohan, A. et al., 2006. Analysis of molecular recognition features (MoRFs). *J. Mol. Biol.*, 362, pp.1043–1059.
Mutka, S.C. & Walter, P., 2001. Multifaceted Physiological Response Allows Yeast to Adapt to the Loss of the Signal Recognition Particle-dependent Protein-targeting Pathway. *Mol. Biol. Cell*, 12(3), pp.577–588.
Ng, D.T.W., Brown, J.D. & Walter, P., 1996. Signal sequences specify the targeting route to the endoplasmic reticulum membrane. *J. Cell Biol.*, 134(2), pp.269–278.
Notredame, C., Higgins, D.G. & Heringa, J., 2000. T-Coffee: A novel method for fast and accurate multiple sequence alignment. *J. Mol. Biol.*, 302(1), pp.205–217.
Ogg, S.C., Barz, W.P. & Walter, P., 1998. A functional GTPase domain, but not its transmembrane domain, is required for function of the SRP receptor beta-subunit. *J. Cell Biol.*, 142(2), pp.341–354.
Ogg, S.C., Poritz, M.A. & Walter, P., 1992. Signal recognition particle receptor is important for cell growth and protein secretion in Saccharomyces cerevisiae. *Mol. Biol. Cell*, 3(8), pp.895–911.
Oldfield, C.J. et al., 2005. Comparing and combining predictors of mostly disordered proteins. *Biochemistry*, 44, pp.1989–2000.
Oldfield, C.J. et al., 2008. Flexible nets: disorder and induced fit in the associations of p53 and 14-3-3 with their partners. *BMC Genomics*, 9.
Oldfield, C.J. & Dunker, A.K., 2014. Intrinsically disordered proteins and intrinsically disordered protein regions. *Annu. Rev. Biochem.*, 83, pp.553–584.
Peluso, P. et al., 2000. Role of 4.5S RNA in assembly of the bacterial signal recognition particle with its receptor. *Science*, 288(5471), pp.1640–1643.
Peluso, P. et al., 2001. Role of SRP RNA in the GTPase cycles of Ffh and FtsY. *Biochemistry*, 40(50), pp.15224–15233.
Rao, M. et al., 2016. Multiple selection filters ensure accurate tail-anchored membrane protein targeting. *eLife*, 5.

Ryan, O.W., Poddar, S. & Cate, J.H.D., 2016. Crispr–cas9 genome engineering in Saccharomyces cerevisiae cells. *Cold Spring Harb. Protoc.*, 2016(6), pp.525–533.
Shan, S., 2016. ATPase and GTPase Tangos Drive Intracellular Protein Transport. *Trends Biochem. Sci.*, 41(12), pp.1050–1060.
Shen, K. & Shan, S., 2010. Transient tether between the SRP RNA and SRP receptor ensures efficient cargo delivery during cotranslational protein targeting. *Proc. Natl. Acad. Sci.*, 107(17), pp.7698–7703.
Shen, K., Zhang, X. & Shan, S., 2011. Synergistic actions between the SRP RNA and translating ribosome allow efficient delivery of the correct cargos during cotranslational protein targeting. *RNA*, 17(5), pp.892–902.
Wang, F. et al., 2010. A chaperone cascade sorts proteins for posttranslational membrane insertion into the endoplasmic reticulum. *Mol. Cell*, 40(1), pp.159–171.
Ward, J.J. et al., 2004. Prediction and functional analysis of native disorder in proteins from the three kingdoms of life. *J. Mol. Biol.*, 337(3), pp.635–645.
Wright, P.E. & Dyson, J.H., 2015. Intrinsically disordered proteins in cellular signalling and regulation. *Nat. Rev. Mol. Cell Biol.*, 16(1), pp.18–29.
Yabal, M. et al., 2003. Translocation of the C terminus of a tail-anchored protein across the endoplasmic reticulum membrane in yeast mutants defective in signal peptide-driven translocation. *J. Biol. Chem.*, 278(5), pp.3489–3496.
Zhang, X., Kung, S. & Shan, S., 2008. Demonstration of a multistep mechanism for assembly of the SRP x SRP receptor complex: implications for the catalytic role of SRP RNA. *J. Mol. Biol.*, 381(3), pp.581–93.
Zhang, X. & Shan, S., 2014. Fidelity of Cotranslational Protein Targeting by the Signal Recognition Particle. *Annu. Rev. Biophys.*, 43, pp.381–408.

Figures Legends

Figure 1. (**A**) Probability of MoRF elements in the SR Linker generated using the sequence analysis software ANCHOR (dashed line), MoRFpred (gray line), and MFSPSSMPred (black line). A schematic representation of the SR Linker is shown above the MoRF probability plot and aligned to the residue index. CBR, RBR, and the predicted MoRF (M) are highlighted. Note that the MoRF partially overlaps with RBR. (**B**) Sequence alignment of the SR MoRF region was generated by T-coffee webserver (Notredame et al. 2000) and plotted using TeXshade package (Beitz 2000). The arrows indicate the four conserved residues R246, W248, L259, Y261 in the MoRF. (**C**) Domain structures of wildtype and mutant SRs used in this study. The transmembrane domain of SRβ was removed to make a soluble SR□□□TM (Lee et al. 2018), which is denoted as SR for simplicity. In SRdL, SRdC, SRdR and SRdM, the deleted sequences are replaced by a $(GS)_6$ linker. (**D, E**) The effects of SR Linker deletions (D) and MoRF point mutations (E) on the co-translational targeting of preprolactin to TKRM. Representative SDS-PAGE-autoradiography images are shown on the left. 'pPL' and 'PL' denote preprolactin and signal sequence-cleaved prolactin, respectively. Translocation efficiencies were calculated from these autoradiographs and their replicates using Eq. 1 in **Methods**. All values are reported as mean ± S.D., with $n \geq 3$.

Figure 2. (**A**) Representative YPD plates showing the growth of *SRP101* and *srp101*^{dM} cells at 30 °C and 37 °C. (**B**) Representative SDS-PAGE-autoradiography images (left) and the quantification (right) of pulse chase experiments to measure the targeting and translocation efficiencies of the SRP-dependent model substrate DHC-□F in *SRP101* and *srp101*^{dM} cells. Successful insertion into the ER results in glycosylation of the substrate (gDHC-□F), which

migrates at a higher molecular weight. Translocation efficiencies were calculated from these autoradiographs and their replicates using Eq. 2 in **Methods**. All values are reported as mean ± S.D., with n ≥ 3 biological replicates.

Figure 3. (**A**) Reaction scheme depicting the GTPase cycle of SRP and SR. SRP and SR are loaded with GTP before their assembly (^{GTP}SRP+SR^{GTP}). As GTP hydrolysis (k_{cat}) is much faster than SRP•SR complex dissociation (Peluso et al. 2001; Lee et al. 2018), SRP-SR association is rate-limiting for k_{cat}/K_m at subsaturating SR concentrations (Fersht 1999). The complex dissociates once GTP is hydrolyzed, releasing free SRP and SR to initiate a new round of the GTPase cycle. (**B**-**D**) Representative SR concentration dependences of the reciprocally stimulated GTPase reactions between SRP and SR for wildtype SR and indicated SR mutants are shown in (B). The lines are fits of the data to Eq. 3 in the **Methods**, and the obtained k_{cat}/K_m and k_{cat} values are reported in (C) and (D), respectively. All values are reported as mean ± S.D., with n ≥ 2.

Figure 4. (**A**) Representative SR concentration dependences of the reciprocally stimulated GTPase reactions of SRP with wildtype or mutant SR in the presence (closed circles) and absence (open circles) of ribosome. The lines are fits of the data to Eq. 3 in **Methods**. (**B**) Summary of the k_{cat}/K_m values from the stimulated GTPase reactions of SRP with wildtype SR or indicated SR mutants, obtained from the data in (A) and their replicates. Solid and open bars denote reactions in the presence and absence of the ribosome, respectively. Values are reported as mean ± S.D., with n ≥ 2. (**C**) Summary of the stimulatory effects of the ribosome on the

k_{cat}/K_m values, calculated from the data in (B). Values are reported as mean ± propagated error, with $n \geq 2$.

Figure 5. (**A**) Representative time courses for dissociation of the SRP•SR complex with wildtype SR (gray) and mutant SRdM (red) in the presence (+80S, closed circles) and absence (–80S, open circles) of the ribosome. The time courses for wildtype SR in the presence of the ribosome were fit to a double exponential equation (Eq. 4 in **Method**), and dissociation rate constants of the fast phase were reported. All other time courses were fit to a single exponential equation (Eq. 5 in **Method**). (**B**) Summary of the dissociation rate constants (k_{off}) of the SRP•SR complex formed with wildtype SR or mutant SRdM in the presence (solid bars) and absence (open bars) of the ribosome. (**C**) Summary of the equilibrium dissociation constants (K_d) of the SRP•SR complex formed with wildtype SR and mutant SRdM in the presence (solid bars) and absence (open bars) of the ribosome. Values of K_d were derived from the equilibrium titrations in Fig. S2C. (**D**) Summary of the rate and equilibrium constants of the SRP-SR interaction for wildtype (WT) SR and mutant SRdM (dM) in the presence (+80S) and absence (-80S) of the ribosome. All values in (B-D) are reported as mean ± S.D., with $n \geq 3$.

Figure 6. (**A**) A representative coomassie-stained gel showing the co-sedimentation of wildtype and mutant SRs with the 80S ribosome. "P" denotes the pellet fraction; "T" denotes the SR used in the total reaction input and was used for normalization. (**B**) Representative coomassie-stained gel (left) and western-blot analyses (right) showing the co-sedimentation of full-length SR and the folded domains in SR with the 80S ribosome. (**C**) Quantification of the efficiency of SR co-sedimentation with the ribosome, based on the fraction of SRα in the pellet fraction relative to

the concentration of SRα in the total reaction mix. All values are reported as mean ± S.D., with n = 2 for SR-X and SR-NG, and n ≥ 3 for all other SR constructs. Replicates of the gel images are shown in Fig. S4.

Figure 7. (**A**) Schematics to show the electrostatic tethering interaction between the GGAA tetraloop of bacterial SRP RNA and basic residues on FtsY, and the corresponding residues in the mammalian SRP and SR. The negative charges of the RNA tetraloop are highlighted as red '–'. The basic surfaces on SR and FtsY are highlighted as blue '+'. The other subunits in the mammalian SRP are shown in light gray and are not labeled for simplicity. (**B**) Summary of the k_{cat}/K_m values for the stimulated GTPase reactions of mammalian SRP and SR with wildtype 7SL RNA and the indicated tetraloop mutants. The values are compared to the published k_{cat}/K_m values for the reactions of *E. coli* SRP and FtsY with wildtype 4.5S RNA and the same tetraloop mutants (Zhang et al. 2008). (**C**) Summary of the k_{cat}/K_m values for the stimulated GTPase reaction of mammalian SRP with wildtype SR and mutant SR(K537A). The values are compared to the published k_{cat}/K_m values for the reactions of *E. coli* SRP with wildtype FtsY and the homologous FtsY(K399A) mutant (Shen et al. 2011). All values in (B) and (C) are reported as mean ± S.D., with n ≥ 3.

Figure 8. (**A**) Free energy profile for SRP-SR complex formation in the presence (left, +80S) and absence (right, -80S) of the ribosome for wildtype SR (black lines) and mutant SRdM (red lines). Activation energies were calculated from the measured dissociation rate constants (k_{off}) and calculated association rate constants ($k_{on} = k_{off}/K_d$) using $\Delta G^{\ddagger} = -RT \ln(k\hbar/k_B T)$, where R = 1.986 cal $K^{-1}mol^{-1}$, T = 298 K, ħ = 1.58 x 10^{-37} kcal s^{-1}, and k_B = 3.3 x 10^{-27} kcal K^{-1}, using a

standard state of 1 μM SR. (**B**) Comparison of the role of the 4.5S RNA tetraloop and the SR MoRF in stabilizing the transition state of SRP•SR complex assembly in the bacterial (upper) and mammalian (lower) SRP pathway, respectively. The membrane-embedded region of SR, 7SL RNA and other SRP subunits are not explicitly depicted for simplicity.

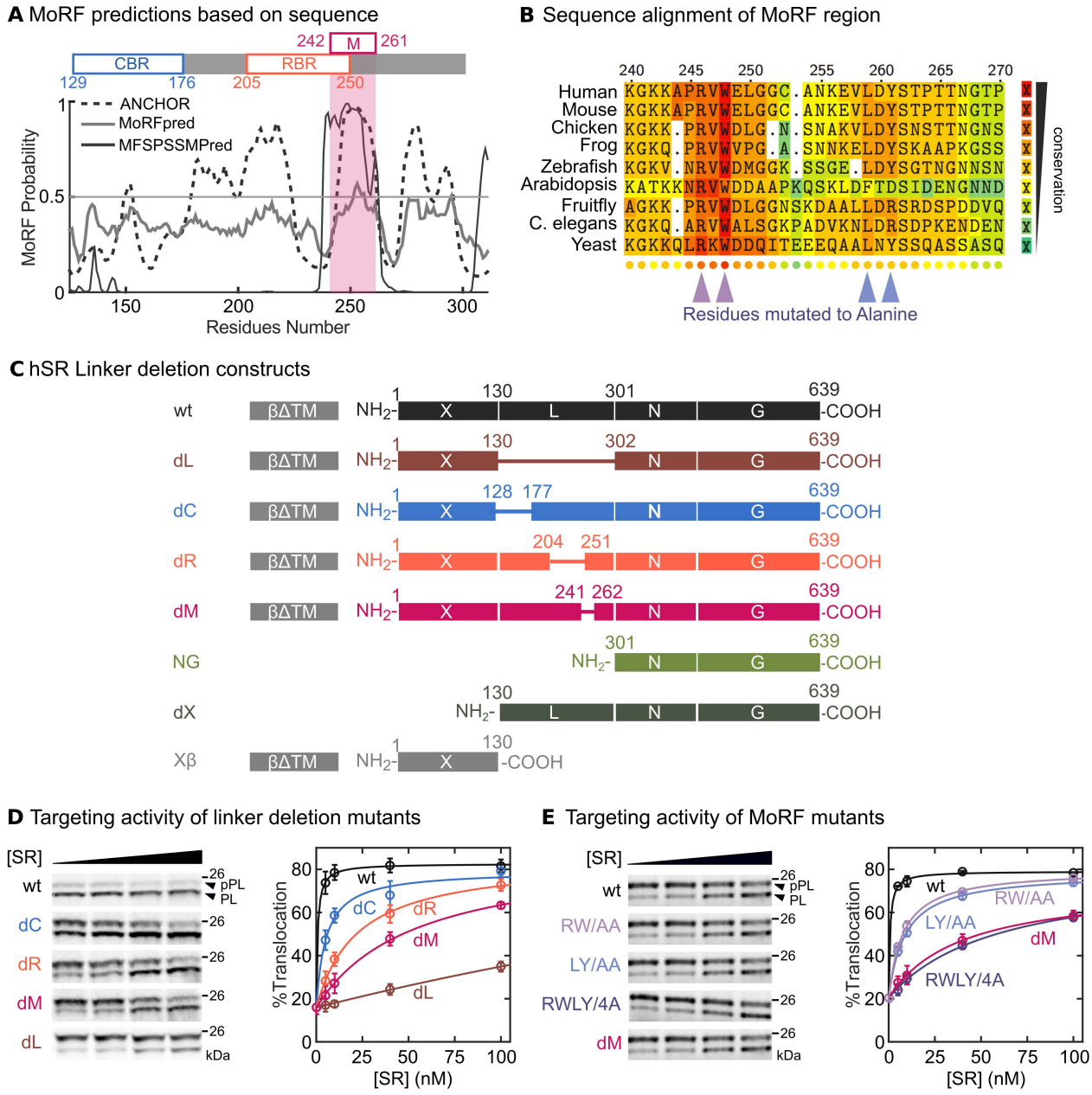
A MoRF predictions based on sequence
242
M
261
CBR
RBR
129
176
205
250
ANCHOR
MoRFpred
MFSPSSMPred
MoRF Probability
1
0.5
0
150
200
250
300
Residues Number
B Sequence alignment of MoRF region
240
245
250
255
260
265
270
Human KGKKAPRVWELGGC.ANKEVLDYSTPTTNGTP
Mouse KGKKAPRVWELGGC.ANKEVLDYSTPTTNGTP
Chicken KGKK.PRVWDLG.N.SNAKVLDYSNSTTNGNS
Frog KGKQ.PRVWVPG.A.SNNKELDYSKAAPKGSS
Zebrafish KGKV.NRVWDMGGK.SSGE.LDYSGTNGNNSN
Arabidopsis KATKKNRVWDDAAPKQSKLDFTDSIDENGNND
Fruitfly AGKK.PRVWDLGGNSKDAALLDRSRDSPDDVQ
C. elegans KGKQ.ARVWALSGKPADVKNLDRSDPKENDEN
Yeast KGKKQLRKWDDQITEEEQAALNYSSQASSASQ
conservation
Residues mutated to Alanine
C hSR Linker deletion constructs
wt
βΔTM
NH2-
1
130
301
639
X
L
N
G
-COOH
dL
302
dC
128
177
dR
204
251
dM
241
262
NG
dX
Xβ
D Targeting activity of linker deletion mutants
[SR]
wt
dC
dR
dM
dL
26
pPL
PL
kDa
%Translocation
[SR] (nM)
E Targeting activity of MoRF mutants
RW/AA
LY/AA
RWLY/4A

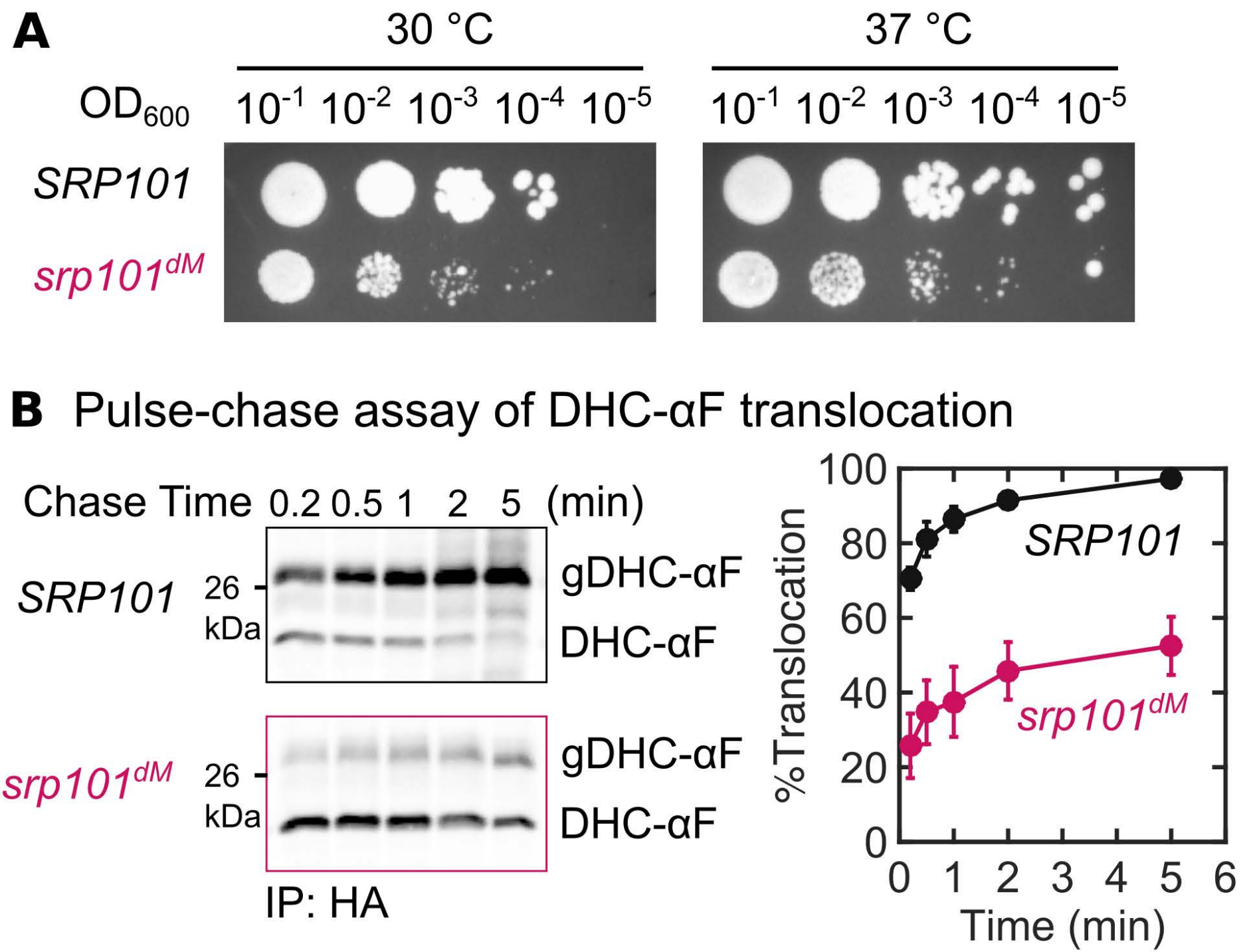
A
30 °C
37 °C
OD600
10-1 10-2 10-3 10-4 10-5
10-1 10-2 10-3 10-4 10-5
SRP101
srp101dM
B Pulse-chase assay of DHC-αF translocation
Chase Time 0.2 0.5 1 2 5 (min)
SRP101
26 kDa
gDHC-αF
DHC-αF
srp101dM
26 kDa
gDHC-αF
DHC-αF
IP: HA
%Translocation
100
80
60
40
20
0
SRP101
srp101dM
0 1 2 3 4 5 6
Time (min)

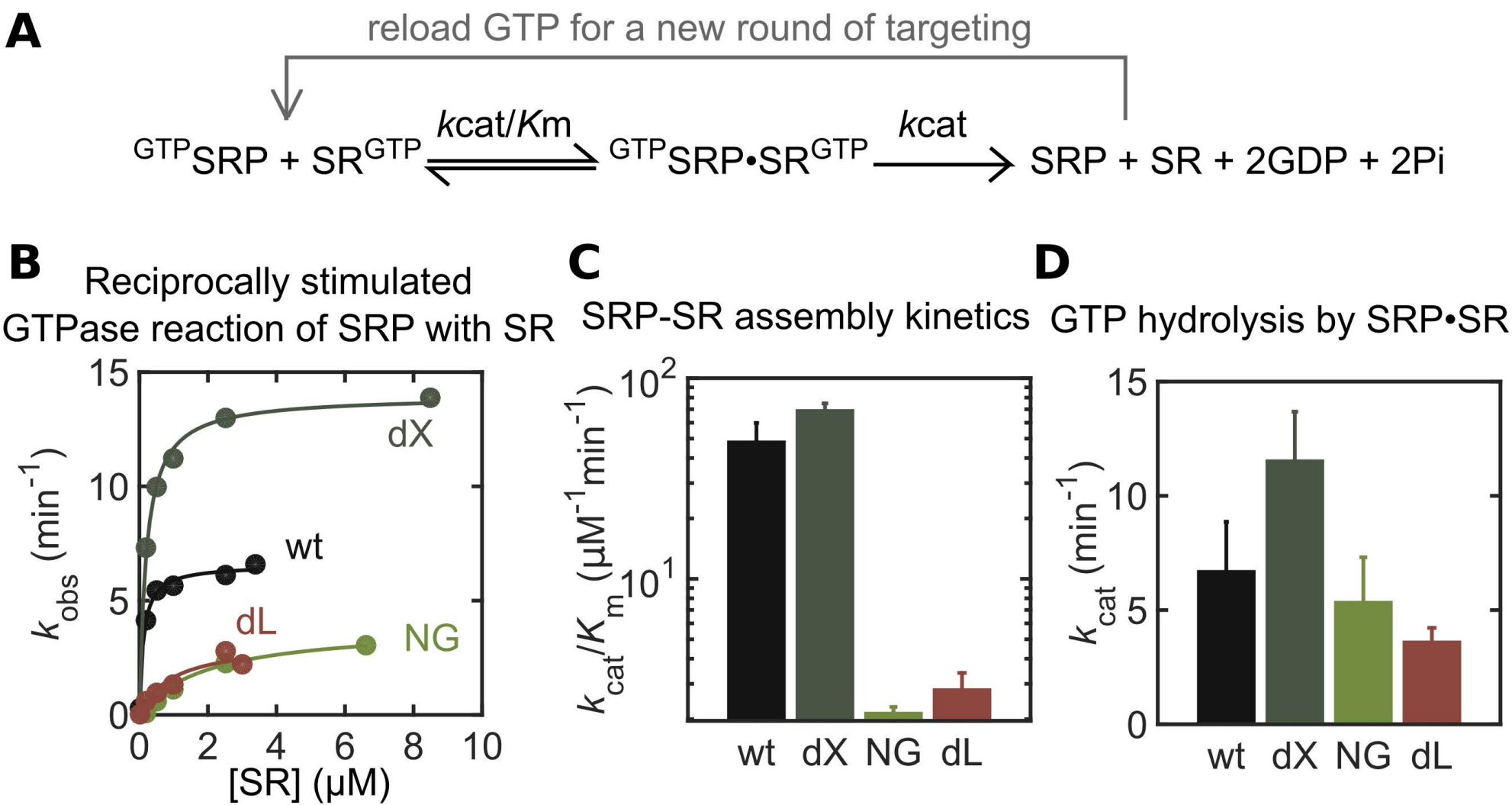
A
reload GTP for a new round of targeting
GTPSRP + SRGTP
kcat/Km
GTPSRP•SRGTP
kcat
SRP + SR + 2GDP + 2Pi
B
Reciprocally stimulated
GTPase reaction of SRP with SR
kobs (min-1)
[SR] (μM)
dX
wt
dL
NG
C
SRP-SR assembly kinetics
kcat/Km (μM-1min-1)
wt dX NG dL
D
GTP hydrolysis by SRP•SR
kcat (min-1)
wt dX NG dL

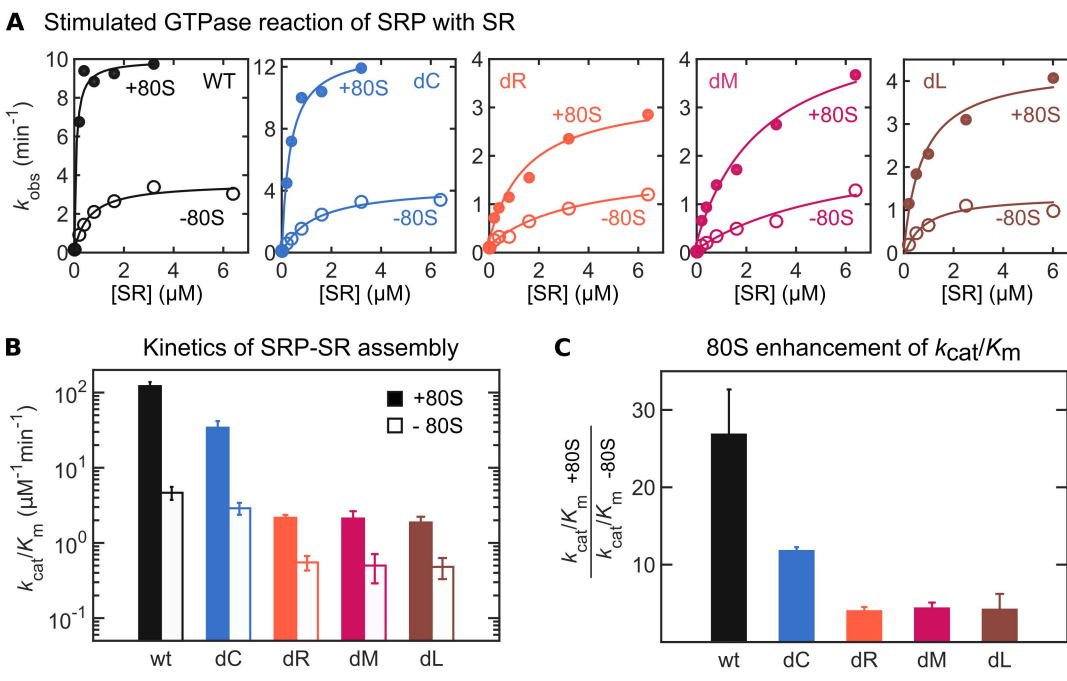
A
Stimulated GTPase reaction of SRP with SR
WT
dC
dR
dM
dL
+80S
-80S
k_{obs} (min^{-1})
[SR] (μM)
B
Kinetics of SRP-SR assembly
+80S
- 80S
k_{cat}/K_m (μM^{-1}min^{-1})
wt
dC
dR
dM
dL
C
80S enhancement of k_{cat}/K_m
$\frac{k_{cat}/K_m\ +80S}{k_{cat}/K_m\ -80S}$

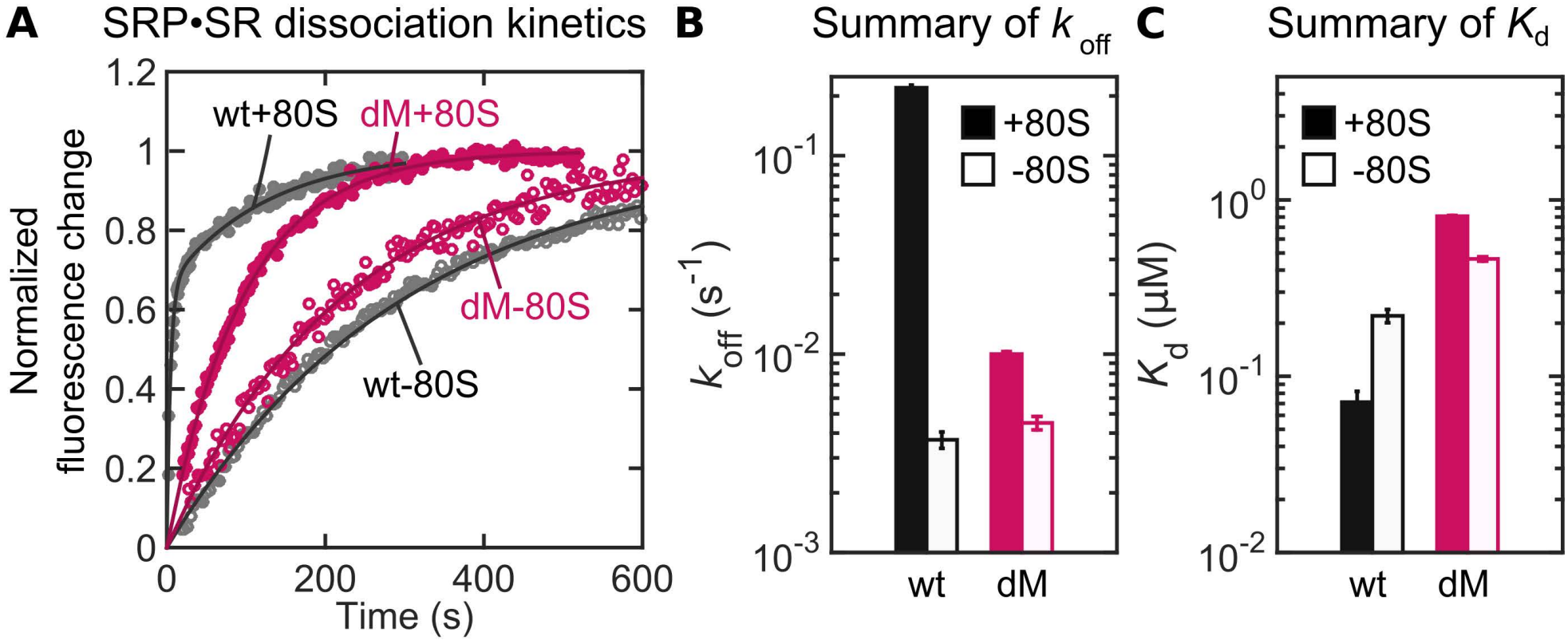

D Summary of the rate and equilibrium constants of the SRP-SR interaction

	+80S		-80S	
	WT	**dM**	**WT**	**dM**
K_d (μM)	0.071 ±0.011	0.809 ±0.008	0.220 ±0.019	0.463 ±0.013
k_{off} (s^{-1})	0.220 ±0.0068	0.010 ±0.0003	3.7 (±0.35) x10^{-3}	4.5 (±0.35) x10^{-3}
k_{on} calculated ($M^{-1}s^{-1}$)	3.09 (±0.48) x10^{6}	1.29 (±0.04) x10^{4}	1.68 (±0.21) x10^{4}	9.72 (±0.81) x10^{3}
k_{on} by k_{cat}/K_m ($M^{-1}s^{-1}$)	2.0 (±0.27) x10^{6}	3.5 (±0.89) x10^{4}	7.8 (±1.5) x10^{4}	8.4 (±3.5) x10^{3}

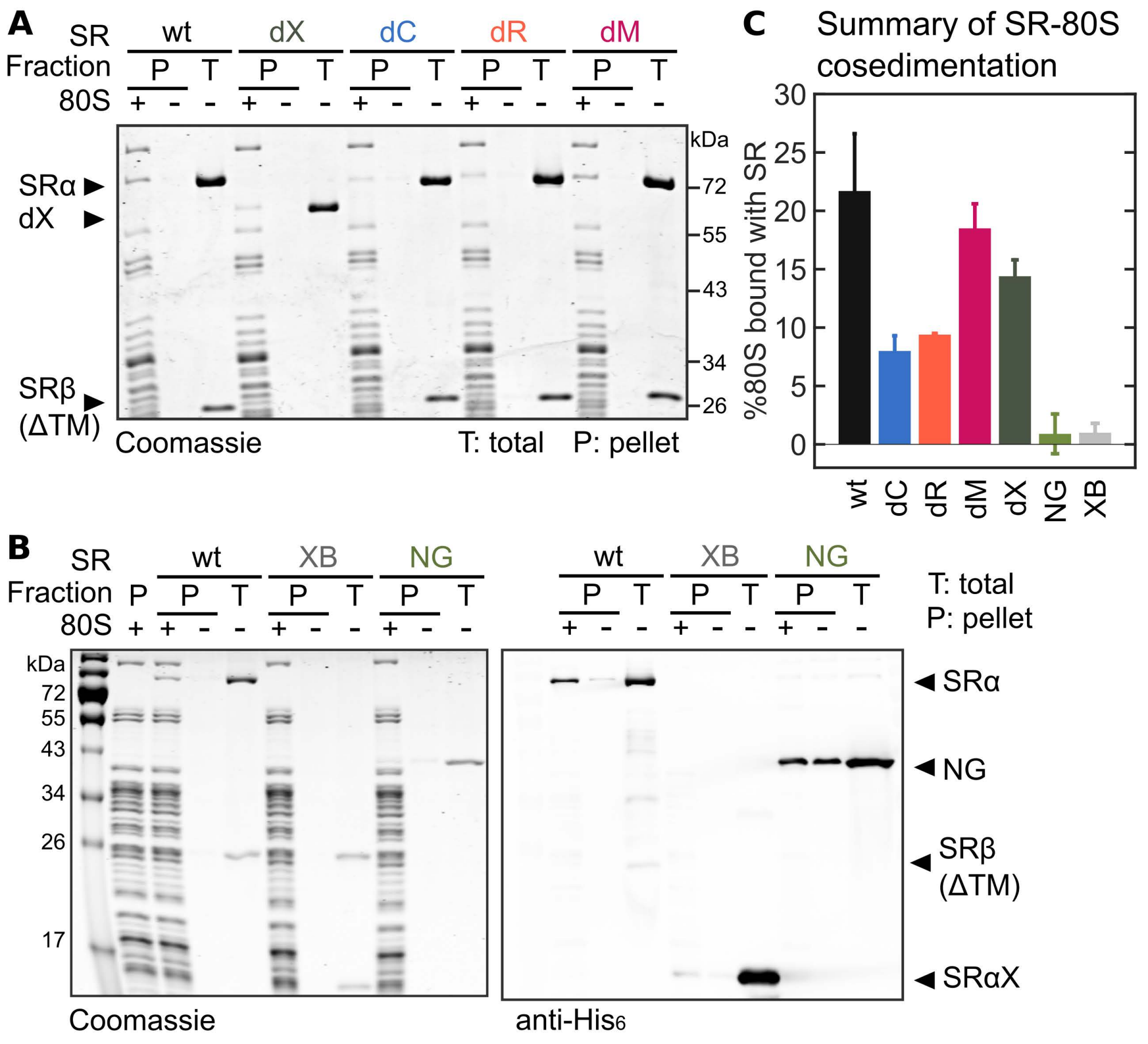
A
SR
wt
dX
dC
dR
dM
Fraction
P
T
80S
+
-
kDa
72
55
43
34
26
SRα
dX
SRβ
(ΔTM)
Coomassie
T: total
P: pellet
C
Summary of SR-80S cosedimentation
%80S bound with SR
30
25
20
15
10
5
0
wt
dC
dR
dM
dX
NG
XB
B
SR
wt
XB
NG
Fraction
P
T
80S
kDa
72
55
43
34
26
17
T: total
P: pellet
SRα
NG
SRβ
(ΔTM)
SRαX
Coomassie
anti-His6

A Comparison of RNA tetraloop and SR charge interactions

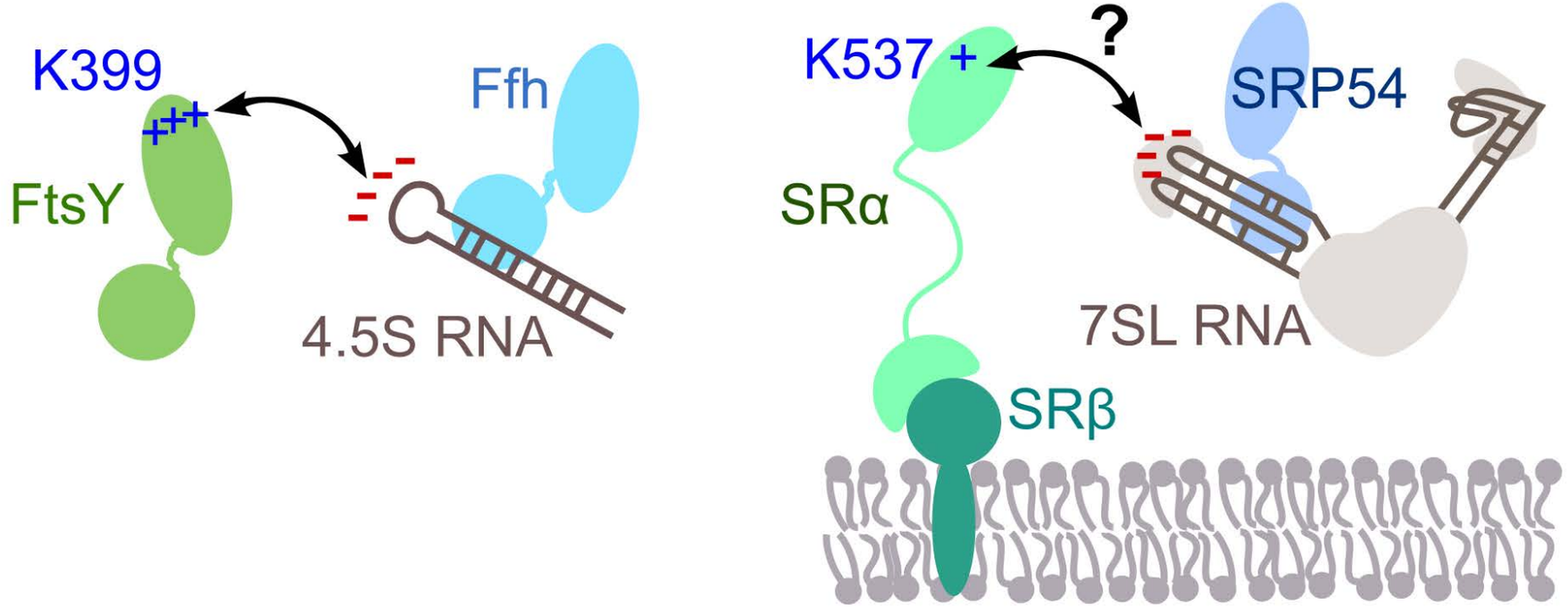

charge tether in *E. coli* SRP

charge tether in mammalian SRP?

B RNA tetraloop mutants

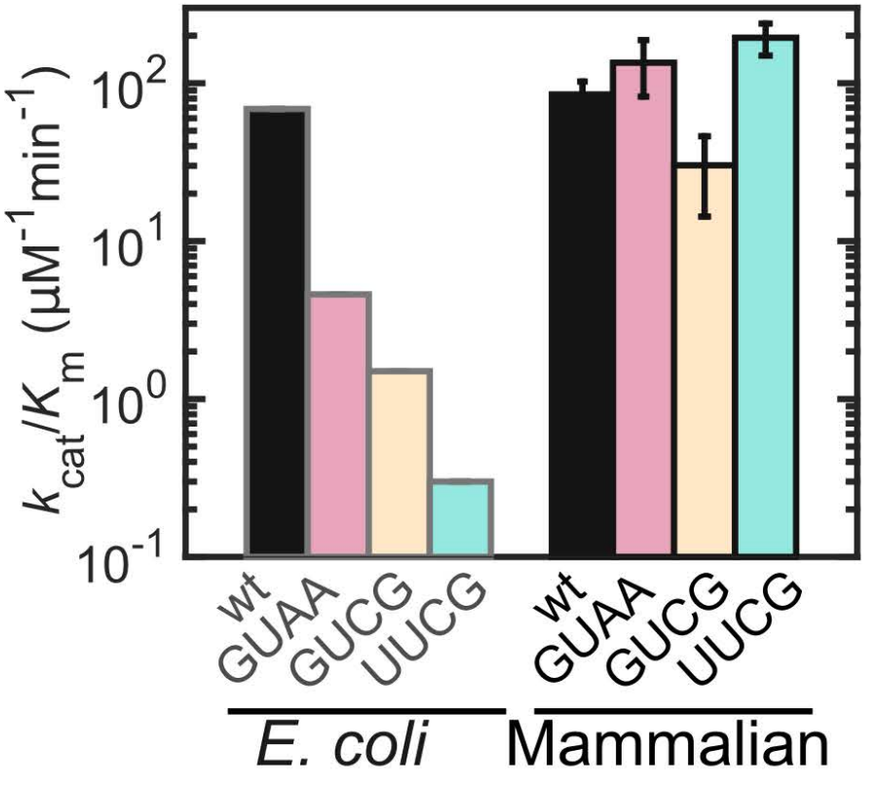

C SR K537(399)A mutants

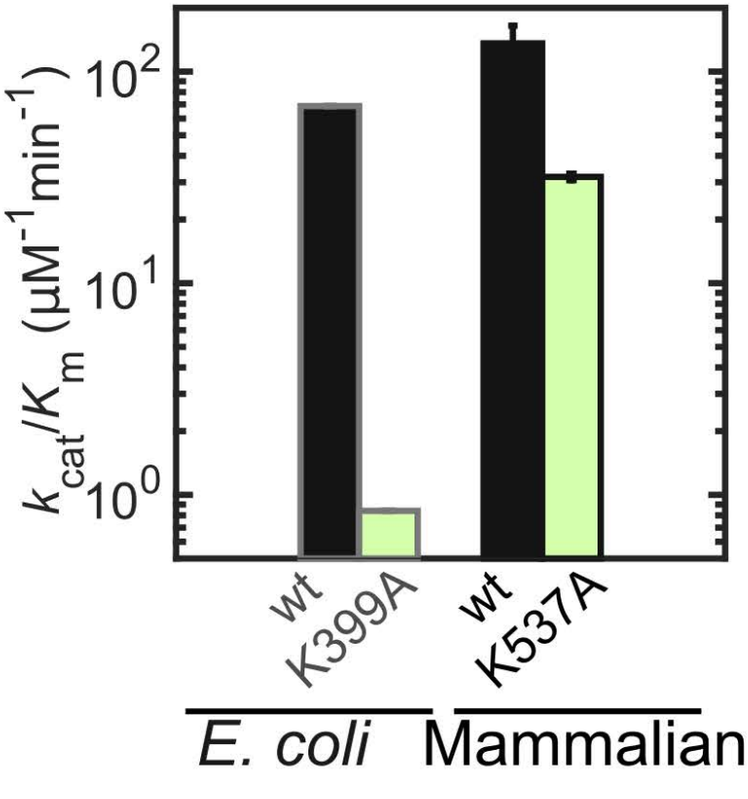

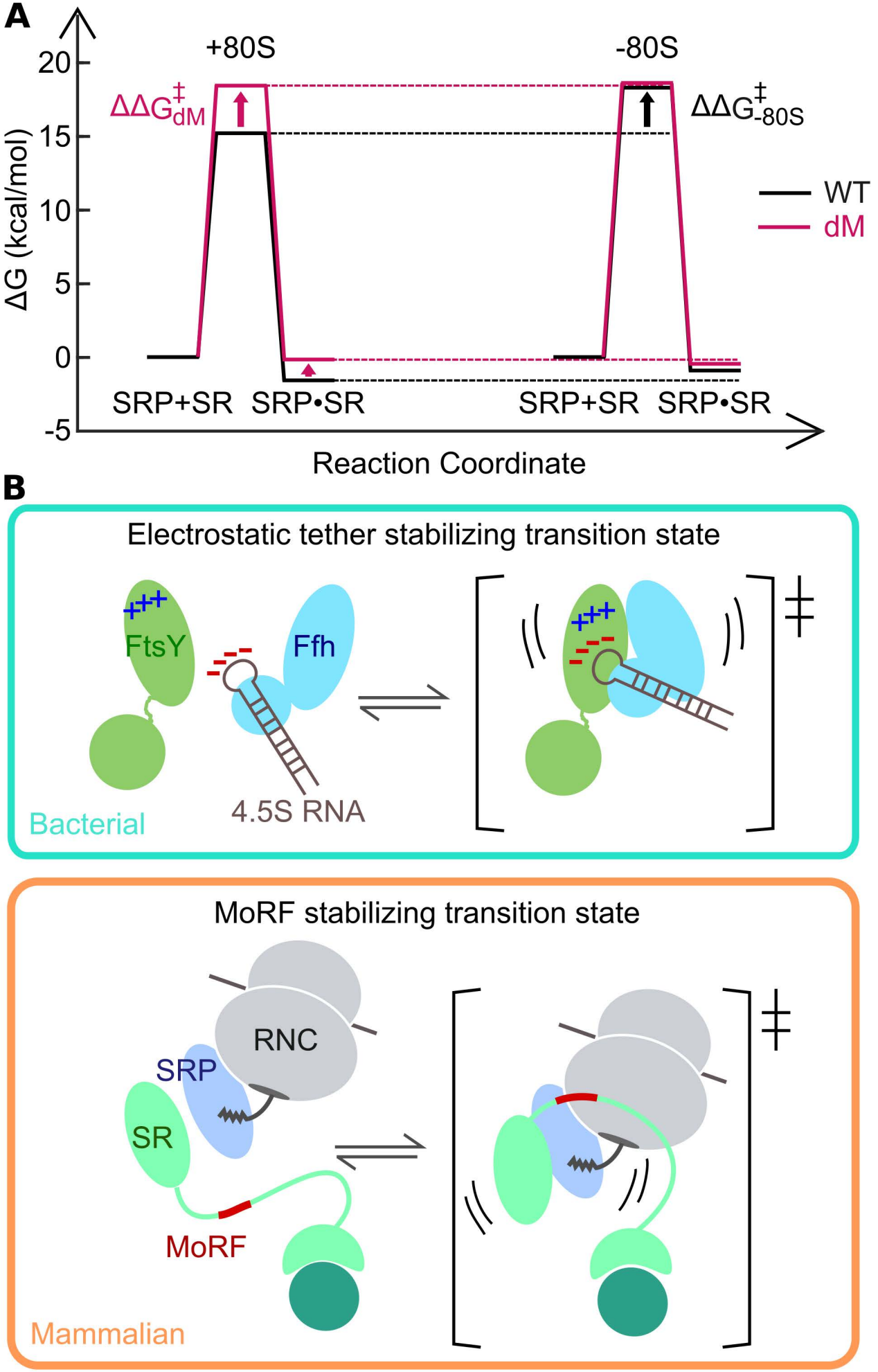
A
+80S
-80S
ΔΔG‡dM
ΔΔG‡-80S
WT
dM
ΔG (kcal/mol)
20
15
10
5
0
-5
SRP+SR
SRP•SR
SRP+SR
SRP•SR
Reaction Coordinate
B
Electrostatic tether stabilizing transition state
FtsY
Ffh
4.5S RNA
Bacterial
MoRF stabilizing transition state
RNC
SRP
SR
MoRF
Mammalian

Supplementary Information for

A Molecular Recognition Feature mediates ribosome-induced SRP-receptor assembly in protein targeting

Yu-Hsien Hwang Fu, Sowmya Chandrasekar, Jae Ho Lee, and Shu-ou Shan*

Division of Chemistry and Chemical Engineering, California Institute of Technology, Pasadena, California, USA

* Corresponding author. Email: sshan@caltech.edu

Key words: Signal Recognition Particle; ribosome; protein targeting; Molecular Recognition Feature; intrinsically disordered protein

Short running title: A MoRF element activates SRP-receptor assembly

Supplemental Figure legend

SI Figure 1. Sequence alignment of full-length eukaryotic SRα generated using T-coffee webserver (Notredame et al. 2000 in the main text) and plotted using TeXshade package (Beitz 2000 in the main text). The CBR, RBR, and MoRF regions in the SR Linker are highlighted in blue, orange, and red, respectively, on top of the sequence index.

SI Figure 2. (**A**) Sequence alignment of full-length human SRα and the yeast homolog, *SRP101*, from *S. pombe* and *S. cerevisiae*, generated using T-coffee webserver (Notredame et al. 2000 in the main text) and plotted using TeXshade package (Beitz 2000 in the main text). The residues with identical amino acid or conservative substitutions are colored according to their chemical properties. (**B**) Replicates of growth assays for *SRP101* and $srp101^{dM}$ cells. (**C**) Western-blot analysis to measure the expression levels of FLAG-tagged SRα in *SRP101* and $srp101^{dM}$ yeast microsomes (50 U/mL), respectively. The band at ~65 kD is a partial proteolysis product of SRα often observed during the preparation and handling of microsomes. "*" denotes a non-specific band. (**D**) Schematics of the model substrates used in the pulse-chase experiments to measure protein targeting. "Y" denotes glycosylation sites. (**E**) Representative SDS-PAGE autoradiography images (left) and the quantification (right) of the ER insertion efficiency for the SRP-independent model substrate BirA-Bos1, measured by pulse chase experiments in *SRP101* and $srp101^{dM}$ cells. Successful insertion into the ER results in glycosylation of the substrate (gBos1), which migrates at a higher molecular weight. Translocation efficiencies were calculated from these autoradiographs and their replicates using Eq. 2 in **Methods**. All values are reported as mean ± S.D., with $n \geq 3$.

SI Figure 3. (**A**) Domain structures of SR Linker deletion mutants based on the SRdX construct used in the FRET measurements. The X-domain is removed to improve protein solubility after labeling. Green symbols denote the C-terminal Sortase tags for fluorescence labeling. Red crosses denote the R458A mutation to block GTP hydrolysis that would drive complex dissociation. (**B**) Summary of the k_{cat}/K_m values of the stimulated GTPase reaction of SRP with wildtype SRdX and indicated SR Linker deletion mutants based on the SRdX construct. Solid and open bars denote reactions in the presence and absence of the ribosome, respectively. Consistent with observations with the SRαβΔTM constructs, the k_{cat}/K_m values of SRdR and SRdM were not stimulated by 80S. The GTPase assays were carried out using the same constructs shown in (A) except for the absence of the R458A mutation. The values are reported from one experiment. (**C**) Equilibrium titrations to measure the binding of SRP to wildtype SR (gray) and mutant SRdM (red) with (closed symbols) and without (open symbols) the ribosome present. All values are reported as mean ± S.D., with $n \geq 3$. Error bars are shown but may not be visible for the data with 80S present.

SI Figure 4. (**A**) Additional coomassie-stained gels showing the co-sedimentation of wildtype and mutant SRs with the 80S ribosome. (**B**) Additional coomassie-stained gel (left) and western-blot analysis (right) showing the co-sedimentation of full-length SR and the folded domains of SR with the 80S ribosome.

SI Figure 5. (**A**) The SR concentration dependences of the reciprocally stimulated GTPase reaction between SR and SRPs assembled with wildtype 7SL RNA or RNAs bearing the indicated tetraloop mutations. All values are reported as mean ± S.D., with $n \geq 3$. (**B**)

Efficiencies of co-translational pPL targeting to TKRM mediated by wildtype SRP or SRPs assembled with the indicated 7SL RNA mutations. All values are reported as mean ± S.D., with n ≥ 3. (**C**) The crystal structures of *E. coli* FtsY (PDB: 4C7O) and *H. Sapiens* SR (PDB: 5L3Q) are shown in electrostatic potential surface (scale ± 2kT/e). The positively charged residues (Lysines and Arginines) in FtsY-NG that interact with the 4.5S tetraloop are indicated, as is the homologous K537 in SR-NG. (**D**) Representative SR concentration dependences of the reciprocally stimulated GTPase reaction of human SRP with wildtype SR (*black*) or mutant SR(K537A) (*green*). The lines are fits of the data to Eq 3, and the k_{cat} and K_m values are reported in Figure 7C.

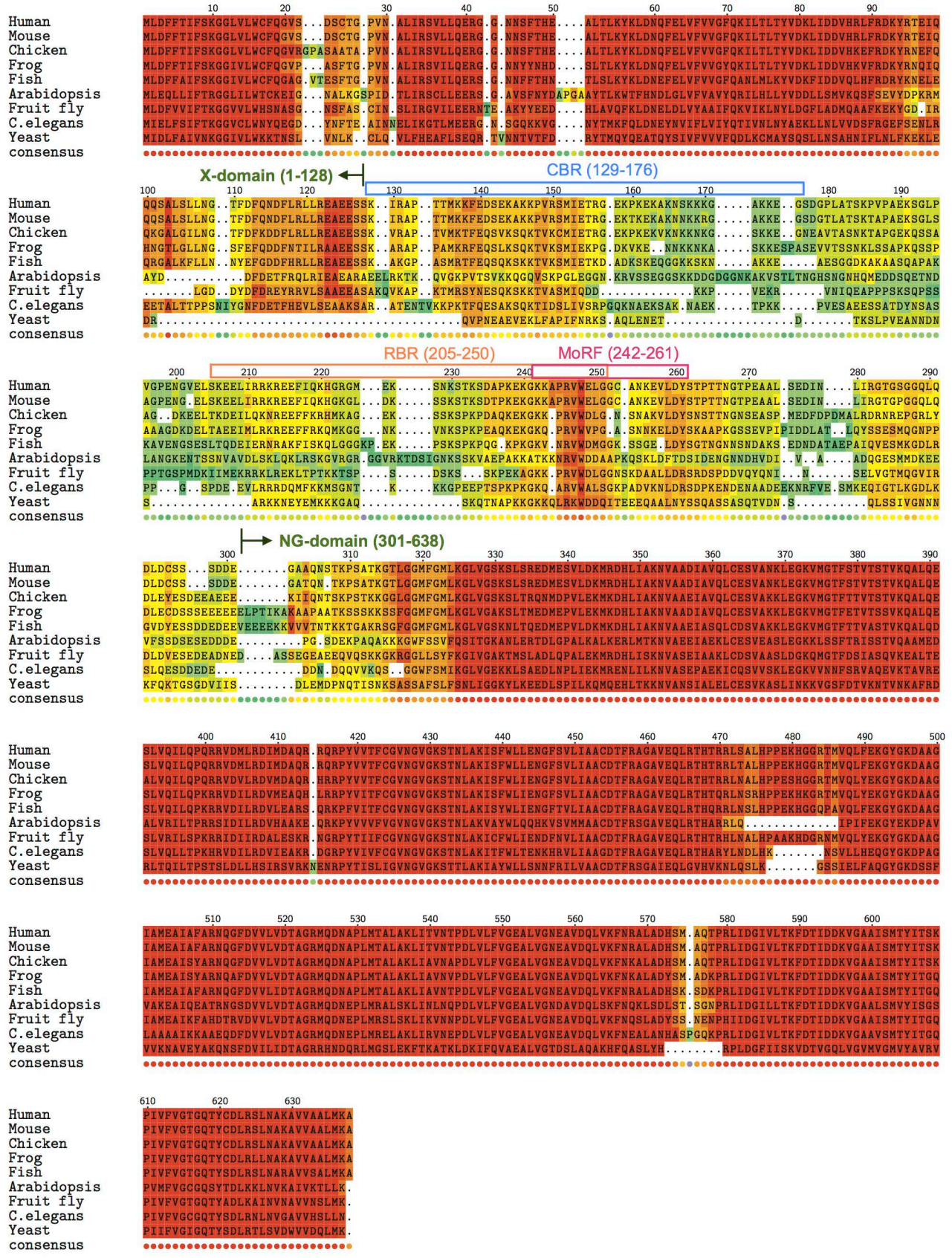
X-domain (1-128)
CBR (129-176)
RBR (205-250)
MoRF (242-261)
NG-domain (301-638)
Human
Mouse
Chicken
Frog
Fish
Arabidopsis
Fruit fly
C.elegans
Yeast
consensus

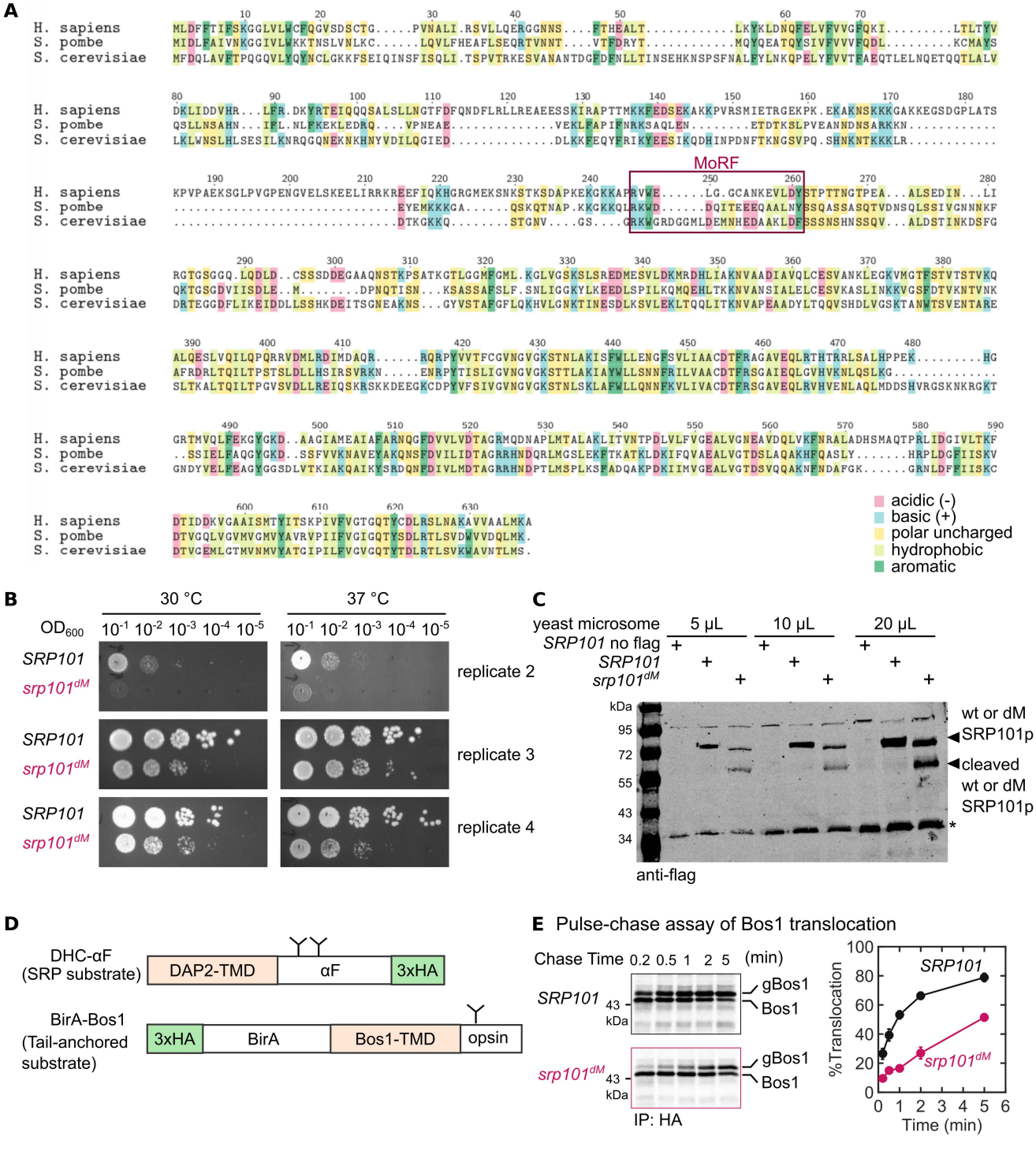
A
H. sapiens
S. pombe
S. cerevisiae
MoRF
acidic (-)
basic (+)
polar uncharged
hydrophobic
aromatic
B
30 °C
37 °C
OD600
10-1 10-2 10-3 10-4 10-5
SRP101
srp101dM
replicate 2
replicate 3
replicate 4
C
yeast microsome
5 µL
10 µL
20 µL
SRP101 no flag
SRP101
srp101dM
kDa
95
72
55
43
34
wt or dM SRP101p
cleaved wt or dM SRP101p
anti-flag
D
DHC-αF (SRP substrate)
DAP2-TMD
αF
3xHA
BirA-Bos1 (Tail-anchored substrate)
3xHA
BirA
Bos1-TMD
opsin
E Pulse-chase assay of Bos1 translocation
Chase Time 0.2 0.5 1 2 5 (min)
SRP101
srp101dM
43 kDa
gBos1
Bos1
IP: HA
%Translocation
Time (min)

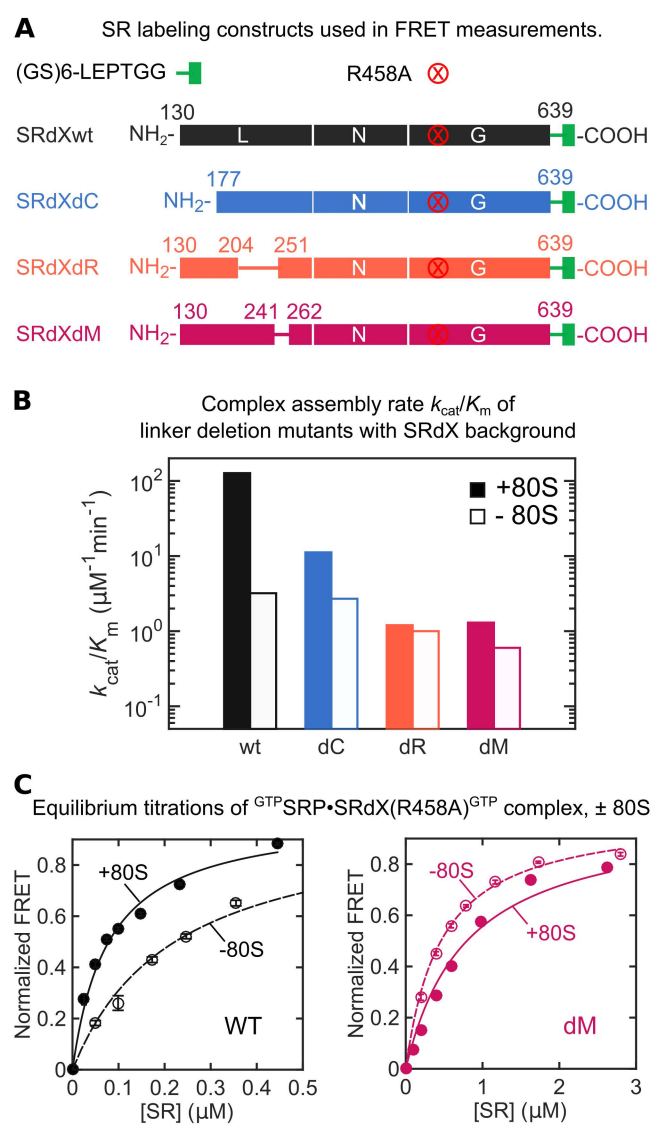
A
SR labeling constructs used in FRET measurements.
(GS)6-LEPTGG
R458A
SRdXwt
SRdXdC
SRdXdR
SRdXdM
NH2-
-COOH
130
177
204
251
241
262
639
L
N
G
B
Complex assembly rate kcat/Km of
linker deletion mutants with SRdX background
kcat/Km (μM-1min-1)
+80S
- 80S
wt
dC
dR
dM
C
Equilibrium titrations of GTPSRP•SRdX(R458A)GTP complex, ± 80S
Normalized FRET
[SR] (μM)
+80S
-80S
WT
dM

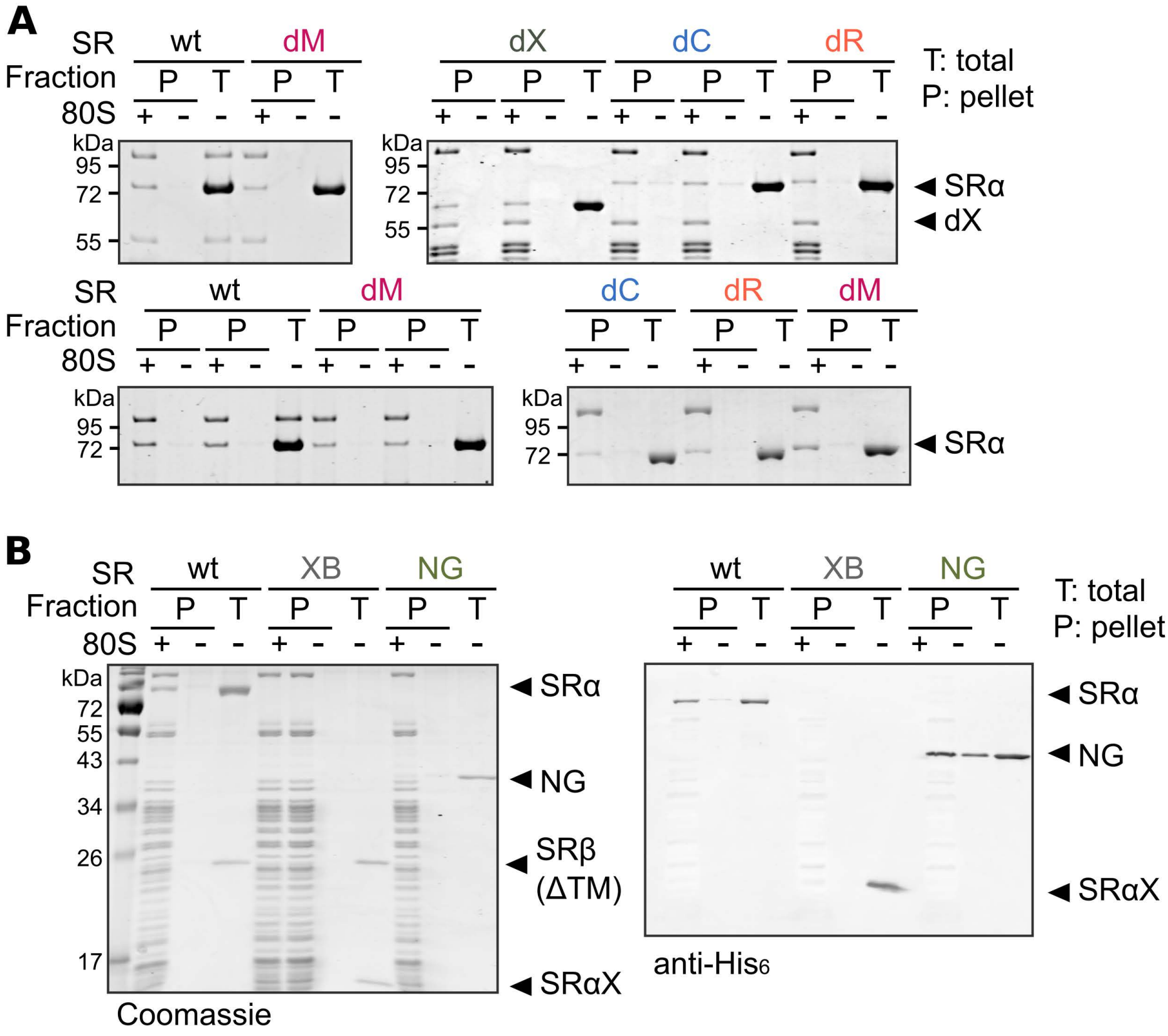
A
SR
Fraction
80S
wt
dM
dX
dC
dR
P
T
+
-
T: total
P: pellet
kDa
95
72
55
SRα
dX
B
XB
NG
43
34
26
17
SRβ
(ΔTM)
SRαX
Coomassie
anti-His6

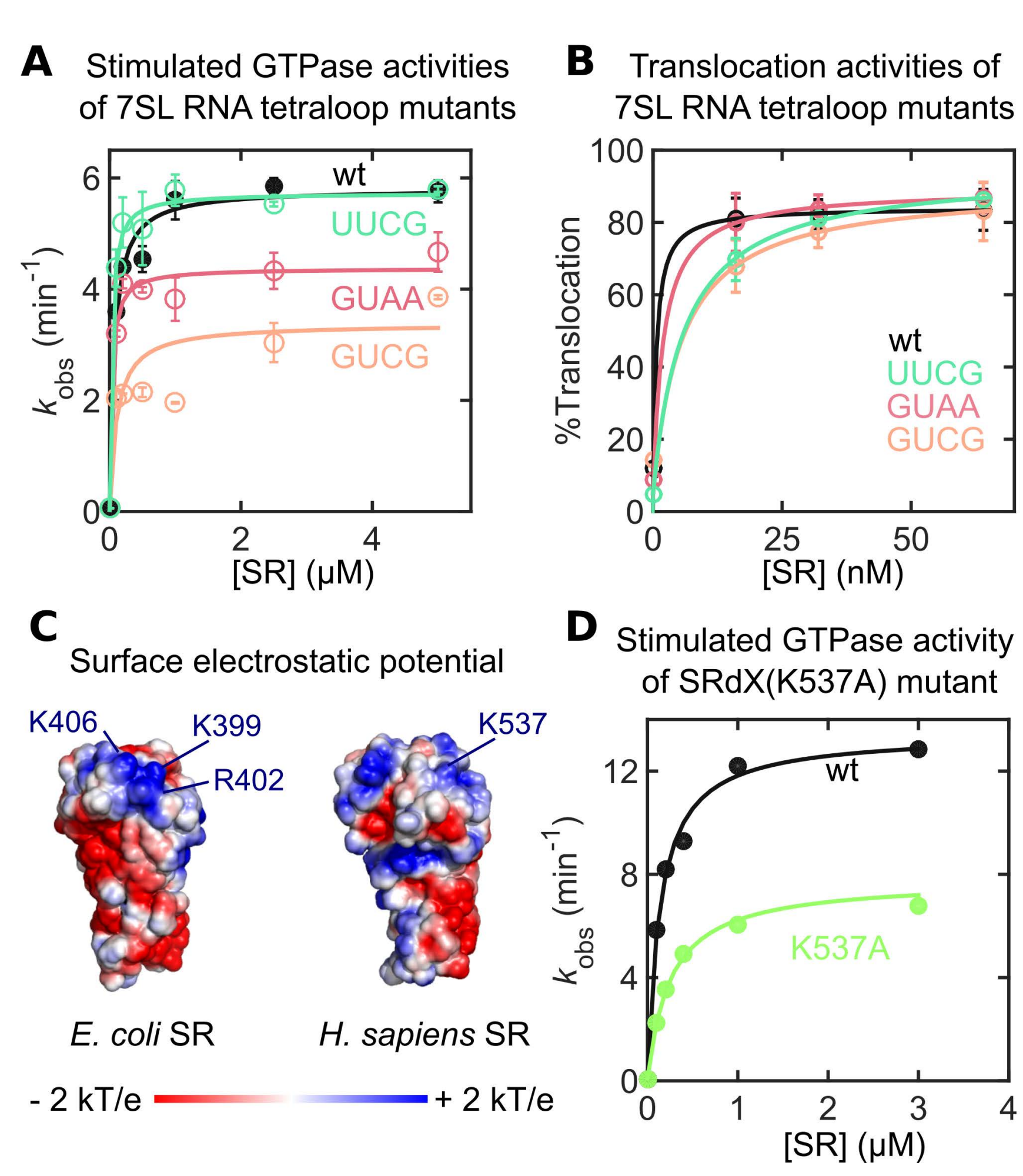
A
Stimulated GTPase activities of 7SL RNA tetraloop mutants
wt
UUCG
GUAA
GUCG
k_{obs} (min^{-1})
[SR] (μM)
B
Translocation activities of 7SL RNA tetraloop mutants
%Translocation
wt
UUCG
GUAA
GUCG
[SR] (nM)
C
Surface electrostatic potential
K406
K399
R402
K537
E. coli SR
H. sapiens SR
- 2 kT/e
+ 2 kT/e
D
Stimulated GTPase activity of SRdX(K537A) mutant
wt
K537A
k_{obs} (min^{-1})
[SR] (μM)